



## Resolving GIA in response to modern and future ice loss at marine grounding lines in West Antarctica

5 Jeannette Xiu Wen Wan<sup>1</sup>, Natalya Gomez<sup>1</sup>, Konstantin Latychev<sup>2</sup>, Holly Han<sup>1</sup>

<sup>1</sup>McGill University, Department of Earth and Planetary Sciences, Montreal, Canada

<sup>2</sup>Harvard University, Department of Earth and Planetary Sciences, Cambridge, Massachusetts

*Correspondence to:* Natalya Gomez (natalya.gomez@mcgill.ca)

10 **Abstract.** Accurate glacial isostatic adjustment (GIA) modeling in the cryosphere is required for interpreting satellite, geophysical and geological records and to assess the feedbacks of Earth deformation and sea level change on marine ice-sheet grounding lines. Assessing GIA in areas of active ice loss in West Antarctica is particularly challenging because the ice is underlain by laterally varying mantle viscosities that are up to several orders of magnitude lower than the global average, leading to a faster and more localized response of the solid Earth to ongoing and future ice sheet retreat and necessitating GIA  
15 models that incorporate 3-D viscoelastic Earth structure. Improvements to GIA models allow for computation of the viscoelastic response of the Earth to surface ice loading at sub-kilometre resolution and ice-sheet models and observational products now provide the inputs to GIA models at comparably unprecedented detail. However, the resolution required to capture GIA in models remains poorly understood, and high-resolution calculations come at heavy computational expense. We adopt a 3-D GIA model with a range of Earth structure models based on recent seismic tomography and geodetic data to  
20 perform a comprehensive analysis of the influence of grid resolution on predictions of GIA in the Amundsen Sea Embayment (ASE) in West Antarctica. Through idealized sensitivity testing down to sub-kilometer resolution with spatially isolated ice loading changes, we find that a grid resolution of  $\sim 3$  times the radius of the load is required to accurately capture the elastic response of the Earth. However, when we consider more realistic, spatially coherent ice loss scenarios based on modern observational records and future ice sheet model projections and adopt a viscoelastic Earth, we find that errors of less than 5%  
25 along the grounding line can be achieved with a 7.5 km grid, and less than 2% with a 3.75 km grid, even when the input ice model is on a 1 km grid. Furthermore, we show that low mantle viscosities beneath the ASE lead to viscous deformation that contributes to the instrumental record on decadal timescales and equals or dominates over elastic effects by the end of the 21<sup>st</sup> century. Our findings suggest that for the range of resolutions of 1.9-15 km that we considered, the error due to adopting a coarser grid in this region is negligible compared to the effect of neglecting viscous effects and the uncertainty in the adopted  
30 mantle viscosity structure.



## 1 Introduction

Changes in sea level in response to ice-mass loss are spatially variable because of glacial isostatic adjustment (GIA), which is the deformational, gravitational, and rotational response of the viscoelastic solid Earth to changes in surface ice and water distribution. The response of the bedrock consists of an instantaneous elastic response of the solid planet's lithosphere and mantle, and a longer timescale viscous relaxation of the mantle towards isostatic equilibrium. GIA models produce predictions of changes in the height of the sea surface equipotential and solid Earth surface (i.e. sea-level changes) in response to surface ice loading changes, which are in turn used to interpret satellite, geophysical and geological records and serve as input to models of ice-sheet dynamics.

Accurate GIA modelling is required to constrain the sea level and solid earth feedbacks on ice dynamics in the coming centuries, especially along unstable marine-grounded ice fronts in Antarctica where bedrock uplift and gravitational drawdown of the sea surface due to ice loss act as a negative feedback to stabilise the retreat of marine-grounded ice-sheet grounding lines (e.g. Gomez et al., 2010; 2013; 2015; De Boer et al., 2014; Konrad et al., 2015; Larour et al., 2019). Furthermore, the GIA response to past and modern ice cover changes makes a significant contribution to satellite records of modern mass changes in marine sectors of the West Antarctica that are actively experiencing ice loss (e.g. King et al., 2012; the IMBIE team, 2018).

GIA modelling in Antarctica is complicated by the fact that the continent is characterised by strong lateral variability in lithospheric thickness and upper mantle viscosity, with low viscosities in the west and high viscosities in the east (e.g. An et al., 2015a; Heeszel et al., 2016; Lloyd et al., 2020). In particular, the low-viscosity mantle and thin lithosphere observed under the West Antarctic Ice Sheet (WAIS) identified from increasingly resolved seismic tomography and geodetic and geologic constraints (Ritzwoller et al., 2001; Morelli and Danesi, 2004; Kaufmann et al., 2005; Nield et al., 2014; Heeszel et al., 2016; Barletta et al., 2018; Shen et al., 2018; Lloyd et al., 2019) leads to a more spatially localised (short wavelength) and faster viscoelastic response to surface loading than cratonic regions covered by Late Pleistocene ice sheets (e.g. Hay et al., 2017; Powell et al., 2020). Over West Antarctica, upper mantle viscosities are thought to vary by several orders of magnitude over short spatial scales reaching as low as  $10^{18}$  Pa s in the Amundsen Sea Embayment (ASE) beneath areas of active marine ice loss (e.g. Nield et al., 2014; Barletta et al., 2018). This implies that viscous effects due to 20<sup>th</sup> century and more recent ice loss will become significant on annual to decadal timescales and accelerate during the timeframe of instrumental records (Barletta et al., 2018; Powell et al., 2020). Viscous effects due to ongoing ice loss also have the potential to influence ice sheet grounding lines in the coming centuries (Gomez et al., 2015) but have not been included in recent high resolution coupled projections (Larour et al., 2019).



To accurately capture the timing and wavelength of GIA effects across Antarctica, models must be capable of both accounting  
65 for 3-D earth structure (i.e., 3-D GIA models such as Latychev et al., 2005 or van der Wal et al., 2015), and be of sufficient  
spatiotemporal resolution to capture the geometry of grounded ice cover. Commonly, GIA, ice-sheet and coupled ice-sheet –  
GIA modelling (e.g. Gomez et al., 2015; Konrad et al. 2015) studies of the sea level change in response to modern and future  
ice loss have been performed with only 1-D (radially varying) Earth structure models (e.g., Kendall et al., 2005; Spada and  
Stocchi, 2007; Adhikhari et al., 2016), or with coarse spatial resolutions of  $> 20$  km due to the computational expense. GIA  
70 models capable of km- to sub-km-resolution have also been developed (e.g. the 1-D GIA model by Adhikhari et al., 2016; the  
3-D GIA model by Latychev, et al. 2005 with updates described in supplementary materials of Gomez et al., 2018). For  
computational efficiency, some of these models implement regional grid refinement techniques which allow for a higher  
resolution along ice retreat margins. Alongside this, improvements in ice-sheet models (e.g. Nowicki et al., 2016; Seroussi et  
al., 2020; DeConto et al., 2021) and observational products (e.g. Studinger, 2014; Bamber et al., 2020; Smith et al., 2020;  
75 Morlinghem et al., 2020) allow similarly high-resolution km- to sub-km- ice thickness and bedrock topography datasets that  
serve as input to GIA models. These advancements allow for GIA models to capture short-wavelength bedrock deformation  
and input ice loading changes at unprecedented detail, but at heavy computational expense, particularly for global 3-D GIA  
models.

80 It is well-established that dynamic ice-sheet models are sensitive to the chosen grid resolution (e.g. Durand et al., 2009; Van  
den Berg & Van de Wal, 2006), requiring km to sub-km resolution to accurately represent ice dynamics and grounding line  
migration in some applications (e.g. Gladstone et al., 2012; Pattyn et al., 2013; Cornford et al., 2016). It has also been suggested  
that as fine as 1-km resolution bedrock topography may be needed to capture the influence of fine-scale topographic features  
on the ice-sheet evolution (Durand et al., 2009) and high resolution may also be needed to represent some embayment walls  
85 and pinning points that act to slow down retreat (e.g. Favier et al., 2012; Joughin et al., 2014; Berger et al., 2016).

While topographic features themselves can be very fine scale, the changes in bedrock elevation and sea level in response to  
ice cover changes tend to be longer wavelength, and the corresponding spatial resolution required to accurately resolve these  
changes in GIA models and their influence on ice dynamics remains poorly understood. Larour et al. (2019) suggested that  
90 kilometer-scale resolution may be required to capture the elastic component of deformation in response to ice loss. However,  
the idealized tests they performed considered an isolated, and increasingly localized load, and their conclusion may not hold  
for more realistic, spatially coherent ice loss scenarios. Furthermore, their model did not include viscous deformation in  
response to ongoing ice loss during the simulation, or account for lateral variations in Earth structure. There have been limited  
studies assessing the length scale of realistic viscoelastic bedrock response beneath the structurally complex WAIS, though a  
95 recent high-resolution bedrock deformation modelling study by Zwinger et al. (2020) suggests a convergence in modelled  
deformation at resolutions finer than 5 km. The broad spatial nature of bedrock deformation and the spatially coherent nature



of ice-sheet retreat, which becomes less localised over longer timescales, suggest that sub-km to km grid resolution, which comes at great computational cost, may not be necessary for accurate GIA model calculations.

100 The aim of this study is to assess the sensitivity of predictions of GIA in response to modern and future ice loss to spatial resolution in the rheologically complex, marine sectors of the WAIS. We build a 3-D viscosity model based on the most recent Antarctic-wide seismic tomography model (Lloyd et al., 2019) to serve as input to a 3-D finite volume, global sea level model (Latychev et al., 2005) to assess the performance of 3-D GIA model predictions across surface grid resolutions of 1.9-15 km. We repeat calculations with a range of Earth models, considering the contribution from elastic and viscous deformation  
105 separately. We focus on the response to observed modern ice loss over the last two decades (Shepherd et al., 2019) and projected future ice sheet retreat in the coming century (Golledge et al., 2019; DeConto et al., 2021) in the Amundsen Sea Embayment of West Antarctica. Our study is motivated by the following questions: What 3-D grid resolution is necessary to adequately capture the elastic and viscous uplift and associated gravitational and rotational effects in response ice loading changes? How significant is the effect of grid resolution compared to sources of uncertainty and simplifications made in some  
110 previous modelling, in particular the neglect of viscous deformation.

## 2 Methods

To investigate the influence of GIA model grid resolution, we first conduct idealized load sensitivity tests over a range of surface grid resolutions from 7.5 to 0.5 km, for the instantaneous removal of cylindrical loads from 0.5 to 16 km in radius  
115 (Section 3). We then widen our “aperture” to assess the model grid resolution required to accurately capture GIA due to modern ice-sheet cover changes from satellite observations (Shepherd et al., 2019) and future ice loss from ice-sheet model projections (Golledge et al., 2019; DeConto et al., 2021) in the rapidly evolving Amundsen Sea Embayment of West Antarctica (Section 4). We choose to locate our study region (light blue square in Fig. 1a) on the ASE both because of the ongoing ice loss and vulnerability to large-scale future marine ice-sheet retreat in the region, and because the region is characterized by low upper  
120 mantle viscosities and a thinned lithosphere (e.g. Barletta et al., 2018) making the ice there sensitive to solid-earth ice-sheet feedbacks. In the ASE, the Pine Island and Thwaites Glaciers together contributed 95 Gt/year of the  $159 \pm 8$  Gt/year total WAIS mass flux in 2017 (Rignot et al., 2019), with studies estimating that collapse of Thwaites Glacier is already underway (Joughin et al., 2014). Accurate GIA predictions are critical to assess rates of future ice-sheet retreat and associated sea level changes making it an ideal location to study the effects of grid resolution on modelled GIA. To represent the radially and  
125 laterally variable Earth rheology in this region, we use a viscoelastic Earth rheology and a range of 3-D viscosity structure models in Antarctica derived from seismic tomography (An et al., 2015a; Heeszel et al., 2016; Lloyd et al., 2019). We adopt a range of 3-D Earth model grids with surface resolutions from 1.9-15 km and compare results to first assess the resolution required to capture the elastic deformation associated with ice loss. Lastly, we repeat these experiments with viscoelastic



130 effects and compare results to the elastic calculations to assess the contribution of viscous effects to modern and future sea level, and the model resolution required to capture these effects. In the sections that follow, we describe the adopted 3-D GIA model, computational grids, Earth rheological models, and adopted modern and future ice loss scenarios.

## 2.1 3-D GIA Model

We compute GIA predictions with a global 3-D finite volume sea level and Earth deformation model (Latychev et al., 2005) capable of regional grid refinement (Gomez et al., 2018). The model solves the sea level equation (Kendall et al., 2005) over  
135 a 3-D global spherical tetrahedral grid defined from the surface to the core-mantle boundary (CMB) that allows us to resolve the laterally and radially varying Earth structure. which are a strong feature in Antarctica. We also adopt this 3-D GIA model because it is capable of regional grid refinement to achieve regional resolution at sub-km scale in regions of interest within a lower resolution globe (Section 2.2). The model computes gravitationally self-consistent solutions for the sea level equation, incorporating effects of time-varying shorelines, Earth rotation changes and viscoelastic deformation of the Earth assuming an  
140 elastically compressible Maxwell viscoelastic rheology. The GIA model requires two main inputs, a 3-D Earth model of viscoelastic rheological properties and a time series of ice thickness changes. These components are described in the following sections. The model also requires global topography as an initial boundary condition, including the elevation of the bedrock beneath the ice. Topography globally outside of Antarctica is set to etopo2 (NOAA National Geophysical Data Centre, 2006) in all experiments with a realistic loading scenario, and the Antarctic bedrock elevation for each of the experiments is described  
145 below.

## 2.2 Computational model grid: regional grid refinement

To compute GIA model predictions, we construct model grids of various surface resolutions (Fig. 1) with the regional grid refinement process detailed in the supplementary material of Gomez et al. (2018). Grid refinement is achieved by incrementally bisecting grid edges in the selected region to achieve a desired resolution, and a final smoothing operation along the region  
150 boundary to ensure a well-behaved transition. We perform calculations on a base grid with a global surface resolution of 15-km, which consists of 20 million nodes and 70 radial layers between the core-mantle boundary and the Earth's surface. The radial layers are defined to respect the unconformities in the radially varying (1-D) seismic reference model STW105 (Kustowski et al., 2008), with the shallowest layers at 12, 25 and 43 km depth. Eight regionally refined grids are constructed from this base grid: five for the idealized load sensitivity tests at 7.5, 3.75, 1.75, 1 to 0.5 km surface grid resolution over a  
155 minimum 0.3-degree radius region around the test load, and three for the more realistic calculations from observed modern and future model projected ice loss, at 7.5, 3.75 and 1.9 km surface resolution in incrementally smaller regions converging over the ASE (Fig. 1). The highest-resolution 1.9 km grid over the ASE has ~ 29 million nodes. As our study focusses on surface grid resolution, the grid refinement is limited to the surface few layers down to ~10 km. Testing with deeper grid refinement during experiment design process indicated that this was sufficient, and our results indicate that km-scale model  
160 resolution is only needed at the surface to accurately capture the geometry of surface loading.



### 2.3 Earth rheological model

The spatial pattern and amplitude of surface deformation in response to ice loading is dependent on the underlying Earth structure. For the idealized sensitivity tests in section 3, we adopt a purely elastic Earth model with a 1-D elastic and density structure. In section 4, we move to a set of realistic simulations using observed or modelled AIS ice loading, adopting 3-D viscoelastic Earth models with a range of viscosity structures constrained by seismic tomography (An et al., 2015a,b; Lloyd et al., 2019) and informed by GNSS-inferences of local mantle structure. The elastic and density structure for these models are based on seismic reference model STW105 (Kustowski et al., 2008). Laterally varying lithospheric thickness (Fig. S1(d)) in all simulations is a composite of a regional lithospheric thickness model by An et al. (2015a) over Antarctica, and a global lithospheric thickness model by Conrad and Lithgow-Bertelloni (2006) everywhere else. Over Antarctica, lithospheric thickness is scaled to have an average of 96 km, resulting in a minimum of 40 km, as was done in Hay et al. (2017).

3-D mantle viscosity variability is estimated from seismic velocity models by scaling isotropic seismic shear wave velocity anomalies to a viscosity variability term using the method developed by Ivins and Sammis (1995). This term defines the variability of mantle viscosity with reference to a chosen 1-D viscosity profile. We follow the same procedure as described in Latychev et al. (2005), Austermann et al. (2013) and Gomez et al. (2018), whereby lateral variations in mantle viscosity are established by sequentially converting the field of relative variations in isotropic shear wave velocity to density, temperature and eventually viscosity anomalies. The final conversion adopts a factor that scales the dependence of viscosity to temperature variations, determining the peak-to-peak lateral variation in viscosity. A different scaling factor is applied to regional and global seismic velocity models to account for the amplitude differences between the different seismic velocity models.

To address the substantial uncertainty in Earth structure, we repeat our simulations with three different 3-D viscosity models: EM1\_L (Figs. 1c, d, S1), EM1\_M, and EM2. EM1\_M and EM1\_L adopt the latest high-resolution 25 km Antarctic seismic tomography model by Lloyd et al. (2019) (ANT-20) in the region south of 45°S and extending from the surface down to the transition zone, and S362ANI (Kustowski et al., 2008) for the rest of the globe. The two variations EM1\_M and EM1\_L were scaled to represent a moderate range of viscosities across Antarctica that match regional averages, and a lower-viscosity endmember adjusted to match GPS-derived inferences of minimum viscosity beneath WAIS (Nield et al., 2014; Zhao et al., 2017; Barletta et al., 2018).

The viscosity variations in EM1\_M are more moderate with scaling factors of 0.0263 for ANT-20 and 0.035 for S362ANI, both close to the preferred value in Kaufmann et al. (2005). These viscosity variations are superimposed on a 1-D viscosity profile of  $5 \times 10^{20}$  Pa s in the upper mantle and  $5 \times 10^{21}$  Pa s in the lower mantle typical in most GIA-based inferences of mantle viscosity (e.g., Mitrovica and Forte, 2004). As noted, the viscosity variations in EM1\_L (Figs. 1c, d, S1) are of higher amplitude



with lower viscosities under WAIS and the ASE. EM1\_L adopts larger scaling factors of 0.033 for ANT-20 and 0.04 for  
195 S362ANI and an accompanying 1-D viscosity profile of  $1 \times 10^{20}$  Pa s in the upper mantle, which is aligned with Lambeck et  
al., (2014) estimates of 1-D upper mantle viscosity using far-field sea-level proxy records, and  $5 \times 10^{21}$  Pa s in the lower mantle.  
The larger scaling factors applied in EM1\_L were calibrated to best reflect the absolute upper mantle viscosity estimates from  
dynamically derived GPS bedrock uplift rates in the WAIS at three locations:  $\sim 6 \times 10^{17}$  to  $2 \times 10^{18}$  Pa s at the northern Antarctic  
Peninsula (Nield et al., 2014),  $\sim 2 \times 10^{19}$  to  $2 \times 10^{20}$  Pa s at the Fleming Glacier in central Antarctic Peninsula (Zhao et al.,  
200 2017), and  $\sim 2.5 \times 10^{18}$  to  $4 \times 10^{19}$  Pa s at the Amundsen Sea Embayment (Barletta et al., 2018). Figures 1c, d and S1 shows  
the resulting low viscosity earth model structure (EM1\_L), which has the lowest viscosity at Marie Byrd land of  $\sim 9 \times 10^{17}$  to  
 $7 \times 10^{18}$  Pa s in the upper mantle.

Lastly, the EM2 model, also adopted in Hay et al. (2017), Gomez et al. (2018) and Powell et al. (2020), is a combination of  
205 three seismic models: S40RTS (Ritsema et al., 2011) globally, a model by An et al. (2015a) in the East Antarctica and Antarctic  
Peninsula, and the model by Heeszel et al (2016) for West and Central Antarctica. The full construction of EM2 is detailed in  
Hay et al. (2017).

## 2.4 Ice model and topography

We consider three ice melt scenarios with resolution ranging from 1- to 5 km in the ASE. The total ice thickness change from  
210 start to end of each scenario is shown in Figs. 2a-c.

For observations of modern ice loss, we adopted a reconstruction we term ICE-SH from Shepherd et al. (2019) of surface  
elevation change ( $\Delta h$ ) from 25 years (1992-2017) of multi-mission satellite altimetry data resolved over a 5-km grid at 5-year  
intervals. We treat  $\Delta h$  as a proxy for ice thickness change (Carrivick et al., 2019), apply the Bedmap2 (Fretwell et al., 2013)  
215 grounded ice mask and saturate ice thickness change  $> 20$  m/yr to control against spurious data points. Initial ice thickness is  
given by Bedmap2. Observations of ice surface elevation changes in Antarctica are continuously improving in resolution, and  
currently range from metre-scale resolution over short observational tracks (e.g. Studinger et al., 2014), to sub-km to km-scale  
resolution at the regional scale (e.g. Bamber et al., 2020), to  $\sim 5$  to 35 km from radar and laser satellite altimetry derived  
records over the whole Antarctic (e.g. Martin Español et al., 2016; Schröder et al., 2019; Shepherd et al., 2019; Smith et al.,  
220 2020). ICE-SH was selected from the available observational datasets due to the 5-km resolution being the highest of its class  
of available satellite altimetry derived-records providing decadal time span surface elevation change records covering the  
whole Antarctic.

For Antarctic evolution over the next century, we apply modelled ice thickness changes from two Antarctic-wide ice-sheet  
225 model projections: (1) ICE-GOL which predicts AIS evolution under RCP 8.5 and including meltwater feedbacks from 2000  
to 2100 at 5-km resolution over 5-year intervals (Golledge et al., 2019), and (2) ICE-RD which predicts AIS evolution from



1950 to 2100 at 10-km resolution over the whole AIS with a nested 1-km resolution simulation over ASE at annual resolution (Extended Data Fig. 5 from DeConto et al., 2021). For ICE-RD, we ran simulations at yearly intervals from 1950-2100 but the interval from 1950-2000 is a period of ice model initialization and we therefore focus on the period between 2000 and 2100 in our results. We also take initial Antarctic bedrock topography from the ice models. Further information of each model can be found in the corresponding references. In selecting these scenarios, the goal is to provide a representative sample of spatially coherent ice-sheet retreat scenarios at high resolution from the literature, rather than to capture all possible projected future ice loss scenarios.

### 3 Idealized experiments: sensitivity of elastic uplift predictions to grid resolution

Our main goal in this analysis is to assess the relationship between grid resolution and elastic GIA predictions, and to identify, for a given load dimension, the grid resolution required to accurately model the associated GIA response. Realistic ice retreat has complex geometry, making it difficult to pinpoint the cause of GIA inaccuracies due to resolution, which may be due to poor representation of the ice load, or numerical errors in representation of the response to Earth loading. To isolate the effect of changing grid resolution on GIA predictions, we first perform a suite of idealized sensitivity tests modelling the instantaneous elastic deformation from unloading of an isolated cylindrical ice load with differing surface grid resolutions that are iteratively bisected from 7.5 km down to 0.5 km. We chose to perform the test with short wavelength, spatially isolated ice loading changes because these would be most poorly represented by a coarse grid compared to coherent ice loss over a broader area. Furthermore, these tests with idealized loads are less computationally costly and enable a systematic assessment reaching higher spatial resolution. In total, 85 GIA simulations were run using 17 ice cylinders of height 100 m and radii ranging from 0.5 to 16 km (0.5, 1, 2, ..., 15, 16), across five different grid surface resolutions: 0.5, 1, 1.75, 3.75 and 7.5 km.

The simulations are performed with the purely elastic 1-D earth model (Sect. 2.3), and an idealized topography of 3800 m south of 24.5 °S and - 835 m everywhere else to reflect the 30:70 land to sea ratio on earth. A radially symmetric ice sheet with steady-state Antarctic ice dome profile (Paterson and Colbeck, 1980) sits on top of this topography extending from the south pole to 69°S, with a maximum height of 3500 m. We also consistently place the centre of the cylindrical load on an arbitrary model grid node in the ASE (76°S 150°W).

#### 3.1 Idealized experiment results

Figure 3 summarises the error in predicted elastic GIA response with varying load radius and grid resolution. Figure 3a shows the bedrock deformation along a transect from the centre of the load for ice cylinders of 2, 5 and 10 km radius, with maximum bedrock uplift predicted on the finest 0.5 km grid of 48, 120 and 185 mm, respectively. Figure 3b indicates whether the grid over- (blue) or under- (red) represents the mass of the load within the model. Errors in the GIA prediction compared to the result for the finest resolution 0.5 km grid (yellow lines) are typically the largest at the load centre where they underestimate



the magnitude of peak displacement. Although a coarser grid may either under- or over-estimate the mass of loading represented in our model (Fig. 3b), it will always dampen the magnitude (effective height) of the load by spreading the load area over a larger grid region. For example, a 5 km radius load will be represented by 3 grid points on a 7.5 km grid, resulting in an overestimated 11.25 km radius loading footprint. For certain radius and grid combinations, the wider load footprint on a coarser grid leads to another zone of peak error occurring outside the load edge (e.g., compare dashed black line to yellow line in Fig. 3a). Even further from the load, the magnitude of deformation decreases and the results from various grid resolutions begin to converge.

These sensitivity test results highlight that the accuracy of predictions depends on the placement of the edge of the load relative to grid nodes and find that the load will be best captured if its edge lies sufficiently close to a grid node (e.g., in Fig. 3b the 1.75 km grid more closely captures the 2 km radius load than the 3 km radius load). Finally, the grid is unable to resolve the load when the grid resolution is more than approximately three times the radius of the load. This is illustrated, e.g., in the black solid line in Fig. 3a, where unloading a 2 km radius load on a 7.5 km grid resulted in no deformation, whereas a 3 km radius load is captured with a 7.5 km grid.

To quantify grid-related error, we calculate the difference between a given simulation and the corresponding simulation with the finest (0.5 km) resolution. We plot the root mean square error (RMSE; Fig. 3c) as an absolute measure of error and the average and standard deviation of the absolute percentage error (Figs. 3d, e) as a relative measure of error, beneath and within 2-km of the loaded region. Fig. 3c shows that the magnitude of RMSE remains relatively constant. This RMSE remained between ~10-20 mm for a 3.75 km grid, and ~20-40 mm for a 7.5 km grid, for example. As the load radius increases, the magnitude of deformation increases as well. However, the error due to grid resolution becomes less significant relative to the total deformation (i.e. the percentage error in Figs. 3d, e decreases).

While the dependence of grid performance on load position relative to grid nodes complicates matters, in order to arrive at an approximate relationship between grid resolution and load size, we assume a linear relationship between the two, which allows us to estimate, for this GIA model, a threshold beyond which grid-related error becomes sufficiently low to no longer merit a further refinement in grid resolution (Figs. 3d, e). For example, in the cross-sectional view of deformation in Fig. 3a, the 10 km radius load deformation is equally well represented by grid resolutions between 0.5 to 1.75 km. Considering the average absolute percentage error (Figs. 3d, e), we found that a 3:1 ratio (represented visually on Figs. 3b-e in the form of a black dashed line) between load radius and grid resolution (6:1 ratio between load diameter and grid resolution) brings the error to  $< 7 \pm 3$  % (where 3% represents one standard deviation of the absolute percentage error calculated within 2 km of the load region).



295 These results provide a rough estimate of the magnitude of error one can expect from a given model resolution and loading scenario, and can serve as a guide for selecting the appropriate grid resolution for a given problem. For example, for an input load with significant isolated locations of ice loss  $\sim 3$  km in radius (or a  $\sim 6$  km in diameter), a grid resolution of 1 km should be adopted. However, these idealized cylindrical load experiments are unlikely to capture the sensitivity of GIA predictions to grid resolution when realistic ice loss geometries are adopted. Such geometries are rarely characterized by spatially localized loads. Furthermore, these experiments capture only elastic deformation and neglect viscous effects, which can be significant on short timescales in low viscosity zones of the West Antarctic. In the following sections we explore how the dependence on grid resolution of GIA model predictions identified here changes when more realistic ice loss geometries and 3-D viscoelastic Earth structure are adopted.

## 300 **4 Results with realistic modern and future ice loss in the Amundsen Sea**

In this section, we consider the importance of grid resolution error for more realistic, spatially coherent modern and future ice loss scenarios. We begin with a consideration of the influence of grid resolution on sea level change in simulations adopting a purely elastic Earth model in section 4.1. Following this, we adopt 3-D viscoelastic Earth models to consider the contribution to sea level change from viscous deformation.

### 305 **4.1 Influence of grid resolution on predictions of elastic deformation**

Figures 2d-f show predicted sea level change in the Amundsen Sea Embayment of West Antarctica adopting an elastic Earth model for three different ice retreat scenarios: one observationally constrained from 20 years of satellite altimetry data from 1997 to 2017 (ICE-SH; Fig. 2a), and two projected from dynamic ice sheet models for the coming century (ICE-GOL and ICE-RD; Figs. 2b-c). Sea level fall is predicted in the entire study region in all scenarios associated with the combination of sea surface subsidence and elastic bedrock uplift due to ice loss – the latter being the dominant signal. Earth rotational effects are included in the predictions but are negligible compared to the other effects in the vicinity of the ice loss. For the modern, the maximum sea level fall from 1992 – 2017 reaches 0.68 m (Fig. 2d), while for future ice loss projections, the sea level fall reaches up to 9.06 m and up to 12.8 m from 2000 – 2100 for ICE-GOL and ICE-RD respectively. Note that in addition to signal coming from local ice loss in the ASE, ice outside this region of interest also contributes a broad signal of smaller magnitude (see Supplementary Section S1).

To explore the resolution dependence of sea level predictions that adopt an elastic Earth model, we repeat the calculations in Figs. 2d-f with a surface grid resolution ranging between 1.9 and 15 km. Fig. 4a-i, shows the difference between results for simulations performed at 1.9 km grid resolution relative to coarser resolutions. The coarser grid simulations tend to underestimate the magnitude of ice unloading and associated sea level fall in most of the domain (red regions in Fig. 4).



The highest grid resolution error occurs at the periphery of the load within a few kilometres of the final grounding line position rather than at the location of maximum deformation (compare Figs. 3d-f to Fig.4) suggesting that the representation of the load is the main source of error rather than the representation of the response of the Earth to the loading. For example, for the ICE-GOL ice loss scenario, the greatest difference between 1.9 and 15 km grid simulations ranges occurs along the entire final grounding line (Fig. 4b), but the maximum sea level fall of over 9 meters occurs ~ 2 km away from the grounding line.

The error decreases with increasing resolution, with minimal differences between the 1.9 km and 3.75 km grid resolutions. The maximum absolute error in the case of a 15 km grid (i.e. the maximum difference between the 15 km and 1.9 km resolution cases) is 44 cm at 2100 in ICE-RD (Fig. 4c), 47 cm at 2100 in ICE-GOL (Fig. 4b) and 9.1 cm after 25 years of modern melt in ICE-SH (Fig. 4a). That is 3.4%, 5.2% and 13% of the peak elastic sea level fall predicted at that time for each respective scenario. The errors are approximately an order of magnitude smaller when a grid resolution of 3.75 km is adopted: 9 cm for ICE-RD, 5 cm for ICE-GOL and 0.7 cm for ICE-SH, or 0.7%, 0.4% and 1.0% of the peak elastic sea level fall respectively.

Since maximum grid resolution error is concentrated along the grounding line for elastic runs, in Fig. 5 we explore how the error evolves during the ICE-RD simulation along a 10-km region bounding the grounding line. The error increases in absolute magnitude with increasing ice loss (“Error” in Fig. 5a; Fig. 5b) but the relative error decreases across the same runs (“Percentage Error” in Fig. 5a). In the case of 15 / 7.5 / 3.75 km grid resolutions, the peak error is ~10 / 5 / 1 cm at the 25 year mark of the simulations, and ~50 / 15 / 5 cm at the 150 year mark (whiskers in Fig. 5a top row). In contrast, the percentage, peaks at 20 / 6 / 1.5% of the signal at 25 years and drops to < 5 / < 2 / < 0.3% after 150 years (Fig. 5a). This decrease in percent error with time reflects that the ice geometry changes become broader in wavelength and can therefore be resolved by a coarser grid compared to the more spatially isolated changes occurring earlier in the simulation. Given the uncertainty in modelled and observed ice loss and bedrock elevation in Antarctica (e.g. Morlinghem et al., 2020), we suggest that for most applications, errors of less than 5% can be achieved with a 7.5 km grid, and errors of less than 2% with a 3.75 km grid.

#### 345 4.2 Contribution of viscous earth deformation to sea level predictions

So far we have focussed on the resolution dependence of the contribution to sea level change from elastic Earth deformation, as this has been a focus of recent literature (Larour et al., 2019). However, the Antarctic Ice Sheet is underlain by strongly laterally varying viscosity structure, and the Amundsen Sea region in particular is underlain by a low viscosity zone and thinned lithosphere (e.g. Barletta et al., 2018; Lloyd et al., 2020). Viscous deformation associated with ongoing ice loss is neglected in Larour et al. (2019) but is expected to be significant on decadal to centennial timescales in this region. In Figs. 2g-i the calculations of sea level change associated with the three ice loss scenarios shown in Figs. 2d-f are repeated with the 3-D viscoelastic Earth EM1\_L described earlier. As with the elastic case, sea level falls beneath regions that experience ice loss in all three cases, but the magnitude of the sea level fall is significantly larger than predictions based on an elastic Earth model (compare Figs. 2g-i to Figs. 2d-f). In particular, peak sea level fall in this case reaches -0.79 m over 25 years in the ICE-SH



355 ice loss scenario, and -14.9 m and -29.1 m from 2000 to 2100 for ice loss scenarios ICE-GOL and ICE-RD, respectively. The  
latter (Fig. 2i) is more than double the sea level calculated with the elastic Earth model (Fig. 2f).

Figure 6a-c shows the contribution of viscous Earth deformation to the sea level predictions, calculated by taking the difference  
between the full viscoelastic calculation shown in Figs. 3g-i and the calculation with an elastic Earth model shown in Figs. 3d-  
360 f. Over the 25 year modern ice loss scenario (Fig. 6a), viscous effects contribute up to 12 cm, or 15% of the peak viscoelastic  
prediction. In the future projections, the viscous contribution reaches up to 6 m of sea level fall, 41% of the peak prediction,  
within 100 years in predictions based on ICE-GOL and up to -17.7 m, or 61% of the peak viscoelastic signal for ICE-RD,  
making viscous effects the dominant contributor over elastic effects in this latter case. For the future projections, compared  
with the elastic signal (Figs. 3e-f), the zones of maximum viscous uplift and sea level fall (i.e. zones of intense red in Figs. 6b-  
365 c) are centered farther out beneath regions that experienced ice mass loss sooner in the simulation and have had more time for  
viscous deformation to occur (Figs. 6a-c), but as we highlight below, substantial viscous deformation still occurs along the  
current grounding line in the simulation. This is less evident in the modern because migration of the location of maximum ice  
mass loss is minimal. Faint blue areas further from the region of ice retreat in Fig. 6b indicate a sea level rise due to peripheral  
bulge subsidence, a viscous process.

#### 370 4.3 Influence of resolution on viscoelastic sea level predictions

In Fig. 7, we repeat the assessment of grid resolution error in Fig. 4, but with a viscoelastic rheology based on the 3-D earth  
model EM1\_L. With the inclusion of viscous behaviour, the magnitude of the grid resolution error is similar to the elastic case  
(compare the range of errors on Figs. 7 and 4) but the spatial pattern of the error becomes more complex. The maximum error  
is no longer solely concentrated along the current grounding line since the solid earth continues to respond viscously to the  
375 poorly resolved loading changes along previous locations of the grounding line. This is particularly evident in the ICE-RD  
simulations where the grounding line retreats across a large area. In this case, the grid resolution error over the region of past  
ice loss and grounding line migration is equal to or larger than the error along the active grounding line (Figs. 7b,c). The error  
increases during the simulation as viscous deformation builds, and thus it also has a dependence on the 3D viscosity structure.

380 Note that in the blue region of Fig. 7c, the sign of the error is not the same as in Fig. 7f because ice retreat is not consistent  
within this particular region in ICE-RD. Specifically, between the years ~2020 to 2050 in ICE-RD, the grounding line in this  
blue region stays relatively fixed, experiencing multiple episodes of localized ice retreat and re-advance (unloading and  
loading). Situations of re-advance tend to occur at lateral scales < 15 km, such that these sub-grid scale movements were not  
adequately captured with a coarser, 15 km grid. Along the final grounding line for ICE-RD, the coarser grids consistently  
385 result in a lower magnitude sea level fall as in the elastic case.



#### 4.4 Earth model uncertainty

To investigate the influence of uncertainty in prescribed mantle viscosity structure, we compare simulations adopting four different earth model configurations: an average 1-D viscoelastic earth model and three 3-D mantle viscosity configurations derived from seismic tomography models (EM1\_L; EM1\_M; EM2; see Methods Sect. 2.3). Figs. 6d-f shows the difference in sea level predicted using the EM1\_L and EM1\_M models, which are based on the same underlying 3-D seismic velocity models but with a varying viscosity scaling factor. EM1\_L (shown in Figs. 6a-c and 2g-i) has the lowest viscosity upper mantle beneath the ASE. Red regions in Fig. 6d-f indicate locations of higher predicted sea-level fall due to lower mantle viscosity in EM1\_L, which results in shorter time scale viscous response. Differences reach up to 5 cm after 25-years with ICE-SH, and up to 2.3 m and 5.8 m between 2000 and 2100 relative for ice loss scenarios ICE-GOL and ICE-RD, respectively, The simulation with EM2, a 3-D mantle viscosity model built from a different seismic tomography dataset, produced deformation with magnitudes intermediate to the simulations with EM1\_L and EM1\_M. We note that the rheological model for this area is uncertain, and our experiments do not comprehensively capture the full range of this uncertainty (see Whitehouse et al., 2020 for a more detailed discussion).

#### 4.5 Time evolution of influence of grid resolution and viscous effects

To compare the relative contributions of grid resolution and Earth model differences over time, we extract predicted sea level time series from all simulations with the ICE-RD ice loading scenario and elastic and viscoelastic Earth models at two locations in Fig. 8: (A) the region experiencing the largest viscous uplift by 2100 (blue star), and (B) the location of maximum ice loss at the 2100 grounding line (red star). Note that the shaded grey region from 1950-2000 in Figs. 8b and c represents a spin up time in the model rather than a realistic representation of the ice cover changes in this region over this time period. In the case of the average 1-D viscoelastic earth model, the sea level response is similar to the elastic case (Fig. 8, compare red and black lines) because the upper mantle viscosity is set to  $10^{20}$  Pa s and thus a significantly longer timescale is required for viscous effects to become significant. Differences between these two simulations and any of the simulations adopting 3-D Earth structure is larger. For example, the differences between simulations using EM1\_L and the 1-D viscoelastic earth model, reach up to 16.5 m and 12.7 m at the sites shown in Figs. 8b and c, respectively, by 2100.

Starting early in the century, the influence of grid resolution becomes smaller than the effect of adopting different Earth models (compare the differences between the dashed and solid lines to differences between different colored lines in Fig. 8). Using the 1-D average earth model (Fig. 8 red lines), viscous effects start to emerge after 50 years and reach only 4% of the peak signal by the end of the run at year 2100. Nevertheless this signal is more significant than the error incurred by using 15 km grid resolution versus of 1.9 km grid resolution by 2040. With a 3-D earth rheology and low viscosities beneath the ASE, viscous effects are pronounced within decades in the simulation (blue and green lines in Fig. 8) and become larger than the



difference in predictions based on 15 km and 1.9 km grid resolutions within 25-30 years and before substantial ice loss has occurred in the simulation.

420 Figure 9 provides a more detailed picture along the grounding line of the contributions to differences in predicted sea level described in the preceding sections. We consider the impact of each factor on the predicted sea level signal at the end of the simulations, plotting the distribution of differences between simulations across all grid points within 10-km of the final grounding line. In interpreting Fig. 9, note once again that in viscoelastic runs, the region of maximum grid-resolution error does not necessarily occur near the grounding line (e.g. Figs. 7c, f). To visualise the distribution, we plot a classic box-whisker  
425 diagram where the boxes represent (from left to right) the 25<sup>th</sup> percentile, median and 75<sup>th</sup> percentile of the distribution, whilst the whiskers represent the “minimum” and “maximum” (25<sup>th</sup> and 75<sup>th</sup> percentiles minus 1.5 times the interquartile range), overlain by a density curve. A box-whisker plot was chosen to mitigate against the effect of outlier points, which we plot as hollow diamonds.

430 Note that the error due to grid resolution consistently has a unimodal distribution that peaks at ~0-1% near the grounding line across a range of durations from 25-years of ICE-SH, to 100 and 150 years (starting from 1950) of ICE-RD. The hollow diamonds show that a significant number of points are statistical outliers, which is likely due to the fact that predicted sea-level change is low in magnitude at some regions along the grounding line that experience less ice-loss, causing even a small magnitude of error to contribute a large percentage error. Inclusive of these outliers, the range of percent error due to a 15-km  
435 grid peaks at ~20% after 25-years of the ICE-SH simulation, but decreases to less than  $\pm 8\%$  by 100-years of the ICE-RD simulation as the magnitude of predicted sea level fall becomes larger across the entire region and the spread of outlier points diminishes. We conclude that the range denoted by the box-whisker plot likely provides a more accurate assessment of the error contributed by each factor in Fig. 9 in zones of active grounding line migration. However, in the following paragraphs we continue to describe the range of errors inclusive of outlier points so as to not under-estimate the possible spread.

440 Our results indicate that the differences due to the choice of adopted Earth model equals and, in most cases, exceeds the size of the error due to grid resolution near the grounding line by the end of all our simulations. Over the 25-year modern observed ice loss scenario, the difference in predictions associated with earth model configuration lies between ~2-10% within 10-km of the grounding line, which is within the range of error due to insufficient grid resolution in a viscoelastic run, which ranges  
445 from  $\pm \sim 20\%$  with a 15 km grid,  $\pm 6\%$  with a 7.5 km grid, and  $< 3\%$  with a 3.75 km grid at all grid points (range of the diamonds outside the shaded distributions in Fig. 9a, though noting the discussion above, the percent error is substantially smaller than these end member values at most points). However, with more ice loss over longer timescales, the difference due to adopted Earth model far exceeds the grid resolution error (Figs 9b, c).



450 If we look beyond the grounding line and consider the difference in predicted sea level between different adopted 3-D viscosity  
models in the entire study region (difference in results with EM1\_L and EM1\_M, plotted in Fig. 6 d-f at 2100), the lower  
viscosity model results in additional viscous deformation that is up to 10.2 %, 21.4% and 20.9 % of the total signal after 25-  
years of ICE-SH, 100-years of ICE-RD and 150-years of ICE-RD respectively. In all cases, the error due to neglecting viscous  
effects far surpasses the error due to grid resolution with a 15-km grid (compare the bottom rows to top 3 rows of Figs 9b and  
455 c)., with the lower viscosity EM1\_L model resulting in an additional viscous deformation that is up to 23.8 %, 58.9 %, 62.4 %  
of the elastic signal near the grounding line after 25-years of ICE-SH, and 100-years of ICE-RD and 150-years of ICE-RD  
respectively.

## 5 Discussion

Our study provides an assessment of the model grid resolution needed to capture decadal to centennial-scale GIA in the vicinity  
460 of active ice loss. We targeted the ASE in West Antarctica as our study location as it is a region with ongoing and projected  
marine ice sheet retreat and where low mantle viscosity and thin lithosphere result in a rapid and localised GIA response to ice  
loading. We adopted a 3-D GIA model to accurately capture the viscoelastic response at high resolution, including the  
complexity introduced by laterally varying earth rheology in the region. Accurate assessments of solid earth deformation from  
past and present ice evolution are important for constraining the negative sea level - solid earth feedback on ice sheet retreat,  
465 and more accurate interpretation of geophysical observables. For the former, our study focusses on the sensitivity of GIA  
predictions along the ice sheet grounding line where this feedback occurs.

### 5.1 Influence of grid resolution

For our suite of simulations with elastic and viscoelastic Earth models, modern and 21<sup>st</sup> century ice loss scenarios, and surface  
grid resolution ranging between 15 and 1.9 km, we found that improvements in the accuracy of model predictions with  
470 increasing grid resolution was limited, remaining within centimetres to decimetres at most at the grounding line. Furthermore,  
our results converged at higher resolutions, with errors from a 3.75 km grid resolution reaching at most 6 cm within 10 km of  
the grounding line in all simulations, even when the input ice sheet model results were available at 1 km resolution in the case  
of ICE-RD. The error introduced in assuming an elastic Earth model and neglecting viscous deformation in the ASE builds to  
an order of magnitude or more larger than the grid resolution error within three to four decades, and up to tens of meters by  
475 the end of the century. In addition, predictions adopting different 3-D Earth models that reflecting the uncertainty in  
viscoelastic Earth structure in the region diverge by up to 1 meter within 50 years and upwards of 2-3 meters after 100 years  
in the simulation.

For coupled ice-sheet - GIA model applications, our results suggest that adopting high resolution in the ice sheet model does  
480 not require a similarly high-resolution GIA model. In our simulations, a 3.75 km grid was sufficient to bring errors to < 2%



along the grounding line for all scenarios (Fig. 9). Furthermore, this percentage decreased over time our simulations, and would continue to decrease multi-century and millennial simulations as the magnitude of viscous deformation and the scale of the ice loss continue to grow. While bedrock topography has smaller scale features (Morlinghem et al., 2020), our results suggest that the GIA signal is less localized and may be computed at lower resolution relative to the ice sheet dynamics and then  
485 interpolated and added to the initial topography on the higher resolution ice sheet model grid, as is done in, e.g., Gomez et al. (2015) and DeConto et al. (2021).

Our results showing that the location of maximum error consistently lies along the load edge for elastic model runs (Fig. 4a-c) suggest that the error due to coarse model resolution is predominantly a result of poor representation of surface ice cover  
490 changes rather than representation of the solid Earth response. For the latter, we would expect the error to occur instead at the location of maximum GIA response (compare differing spatial patterns in Fig. 2e, f to 4b, c). When the viscous response is incorporated, the time-evolving nature of viscous deformation leads to an additional peak in grid resolution error at locations past the grounding line due to inaccurate representation of past loading (Fig. 7). This additional zone of error will not affect active ice sheet grounding lines (though it may be important for interpretation of modern records), and while the spatial pattern  
495 of the error differs, the magnitude of the error due to grid resolution was similar across both elastic and viscoelastic simulations.

Our findings on the size and source of resolution error are in contrast to recent work by Larour et al., (2019) who suggested that kilometre resolution was required to capture elastic deformation. This discrepancy may be due in part to Larour et al. (2019) considering only point loads in their idealized resolution experiment, while our conclusions are based on more realistic,  
500 spatially coherent ice loss scenarios. Differences may also arise due to the nature of the computational grid and processing of inputs (see section 5.3) which should be explored in more detail in future GIA model inter comparison efforts. Nevertheless, our predictions based on an elastic Earth model converge to theirs for more spatially broad loads.

One possible limitation in this study is we do not reach sub-km grid resolution in our GIA model, and our highest resolution  
505 ice model is 1 km. In sensitivity tests with idealized loading scenarios in Section 3 we adopted a grid resolution as low as 0.5 km grid and found that a minimum 1:3 ratio between grid resolution and load radius was required for results to incur an error of  $< 5 \pm 3$  ( $\sigma$ ) % along the load edge, suggesting that a 3.75km grid would be unable to capture a spatially isolated,  $< 1$  km radius ice unloading event. That we did not see significant error at this resolution in the realistic simulations indicates that the ice cover changes are spatially coherent and there are no significant spatially isolated ice unloading events (i.e. no ice thickness  
510 changes occurring over only a few grid points) predicted in the 1-km resolution ICE-RD ice model simulation (Fig. 5).

To further investigate if short-wavelength, spatially isolated ice loss scenarios exist over Antarctica, we assessed the surface elevation change observables from 40 and 25 years of multi-mission satellite altimetry data by Schröder et al., (2019) and Shepherd et al. (2019) respectively, and 15 years of airborne laser altimetry from Operation IceBridge (OIB ATM L4;



515 Studinger, 2014 (Updated 2018)). While a more detailed investigation is merited, in our initial analysis of these datasets we  
observed that spatially isolated ice loss events have a lower magnitude, only persist over short timescales, and found no  
evidence of high magnitude, short-wavelength ice loss occurring with spatial scales  $< 5$  km. Thus, we expect that spatially  
isolated ice unloading occurs rarely and will not have a significant impact on the overall accuracy of GIA model results in a  
given region. Nonetheless, with improving observational products and ice sheet model resolutions, we expect to obtain  
520 regional-scale ice loading grids of sub-km resolution that may warrant further study with a sub-km GIA model grid (e.g. Durkin  
et al., 2020).

## 5.2 Influence of viscous deformation and earth model uncertainty

Within decades in the ASE, viscous deformation is a significant contributor to the GIA signal (Hay et al., 2017; Barletta et al.,  
2018; Powell et al., 2020; Kachuck et al., 2020). The GIA response can be decomposed into the following: perturbation of the  
525 sea surface equipotential, elastic deformation and viscous deformation of the solid earth surface. Previous studies have isolated  
the GIA signals from each of these components to assess the relative importance of each factor on ice sheet dynamics. Over  
decadal to centennial timescales, Larour et al. (2019) show that purely elastic deformation was more significant than the sea  
surface perturbation on continental-scales, while Kachuck et al. (2020) found that viscous deformation is more significant than  
either elastic deformation or the perturbation to the sea surface. In this study, we have confirmed that viscous deformation  
530 effects are significant within decades, particularly in the low viscosity region of the ASE, where the viscous component of  
deformation can reach multi-metre scales by the end of the century. This body of work highlights the importance of  
incorporating viscous behaviour in GIA modelling applications in regions of low mantle viscosity.

Complicating efforts to accurately characterise the viscous deformation behaviour is the uncertainty in Earth's viscosity  
535 structure. The timescale of viscous solid-earth deformation on ice sheet dynamics is strongly dependent on the assumed earth  
rheology. The global average mantle viscosity of  $\sim 10^{21}$  Pa s (Forte and Mitrovica, 1996) corresponds to response times from  
centuries to millennia, whilst recent seismic (Lloyd et al., 2020) and GPS observations suggest an upper mantle viscosity under  
the ASE as low as  $\sim 10^{18}$  Pa s (Barletta et al., 2018). Rapid viscous uplift response was similarly identified in Kachuck et al.  
(2020) which used a 2-D GIA model of mantle viscoelastic deformation and found that sea level fall associated with  
540 viscoelastic mantle deformation led to a 30% reduction in modelled ice sheet volume loss by 2150. Our study compares results  
generated with three 3-D earth rheology models; EM1\_M and EM2 have a comparable viscosity range, while EM1\_L has the  
lowest viscosity values under the ASE. These results demonstrate that uncertainties regarding the effective mantle viscosity  
are significant and can contribute up to multiple metres of uncertainty by the end of a 100-year simulation (Fig. 6). Furthermore,  
additional uncertainty arises from the model of viscoelastic behaviour. We adopt a viscous Maxwell rheology, but studies  
545 suggest that incorporating a short-term transient component of deformation may result in even faster viscous deformation (e.g.  
Pollitz, 2019).



### 5.3 On GIA model setup

In choosing a method for representing a finer resolution load grid onto a coarser model grid, we found that it is important to consider how the model itself discretizes the load, and the input load interpolation schemes. Here, it is worth noting that our  
550 GIA model grid is a tetrahedral grid (triangular grid on surface), and these findings may not translate perfectly to other model  
grid compositions. Our GIA model grid consists of a uniform global tetrahedral grid that allows for regional patches of refined  
resolution (also uniform) but does not permit matching of model grid nodes to the input grid. For our experiments, by  
comparing the volumes of the input ice calculated on the input and GIA model grids, we found that the in-built Poisson  
interpolation scheme (Latychev et al., 2005) performed better in interpolating the finest resolution load grid onto the model  
555 grid compared to other tested schemes, suggesting that an understanding of the method in which the load is mapped onto the  
model grid nodes is important. Additionally, we note that considerations such as the resolution of the input ice sheet model  
and treatment of the ice cover outside the region of interest also have an influence on the final GIA model predictions (see  
Supplementary Section S1) and should be explored further in future studies.

### 6 Conclusion

In this study, we present a comprehensive analysis of the influence of grid resolution on modelled GIA effects in response to  
ice cover changes over the modern satellite era and through the 21<sup>st</sup> century. We adopt a range of Earth models including  
models that capture lateral variations in Earth structure based on seismic tomography and GNSS analyses. These experiments  
showed that: (1) the grid resolution error introduced through adopting a 15 km grid relative to a 1.9 km model grid remains  
within centimetres to decimetres throughout our simulations; (2) the grid resolution error is the highest along load edges for  
565 purely elastic deformation cases, and along past and current grounding line positions for viscoelastic Earth models, and is  
primarily associated with the representation of the surface load; (3) results with grid refinement beyond 3.75 km converged in  
our simulations, even when adopting a 1 km resolution input load, and this likely represents a conservative lower bound since  
the next coarser grid we considered was 7.5 km. The errors associated with the choice of grid resolution will decrease with  
time for longer simulations as the extent and magnitude of ice loss and associated GIA response increase. Furthermore,  
570 comparison of simulations adopting elastic and 3-D viscoelastic Earth models demonstrate that the contribution of viscous  
deformation can be up to tens of metres over the 21<sup>st</sup> century, or > 50% of the total deformation signal. Additionally,  
uncertainties in earth properties can contribute up to several metres of error. This indicates the importance of considering  
viscous uplift when modelling GIA over decadal to centennial timescales in the ASE. In comparison, the error due to grid  
resolution is negligible for grids of spacing of 3.75 km and less.

575

To supplement these findings with realistic loading, we conducted a sensitivity test with cylindrical loads with radii from 16  
km to 0.5 km and grid resolutions from 7.5 to 0.5 km. These indicate a minimum 1:3 ratio between the required grid resolution  
and the load radius (or 1:6 with load diameter) to minimise grid resolution error. However, no significant spatially isolated



loads occur in our adopted observation- and model-based ice loss scenarios, and a preliminary examination of other ice  
580 observation and modelled products suggest that significant ice loss with  $< 5$  km wavelength is rare in the ASE. These results,  
taken together, support the conclusion that km-scale resolution in GIA modelling is generally not necessary. However, as  
higher resolution sub-km ice observational and dynamic ice model grid products are released, this guidance may have to be  
revisited.

### Code/Data Availability

585 We will make all model output from the sensitivity tests and more realistic simulations available on a public repository. The  
3-D GIA model adopted here has been used in numerous previous studies, questions regarding the model or requests for  
additional output can be discussed with the corresponding author and K.L., the developer of the code. Additional data related  
to this paper may be requested from the authors.

### Author Contribution

590 J.X.W.W. and N.G. developed the ideas and experiments in the study with input from K.L. and H.K.H.. K.L. contributed to  
designing the experimental set up. J.X.W.W. performed the simulations and analysis. J.X.W.W. and N.G. wrote the original  
text and all authors contributed to revisions.

### Competing interests

595 The authors declare they have no competing interests.

### References

- Adhikari, S., Ivins, E. R., and Larour, E.: ISSM-SESAW v1. 0: Mesh-based computation of gravitationally consistent sea-  
level and geodetic signatures caused by cryosphere and climate driven mass change, *Geoscientific Model Development*, 9,  
1087-1109, <https://doi.org/10.5194/gmd-9-1087-2016>, 2016.
- 600 An, M., Wiens, D. A., Zhao, Y., Feng, M., Nyblade, A. A., Kanao, M., Li, Y., Maggi, A., and L  v  que, J. J.: S-velocity model  
and inferred Moho topography beneath the Antarctic Plate from Rayleigh waves, *Journal of Geophysical Research: Solid  
Earth*, 120, 359-383, <https://doi.org/10.1002/2014JB011332>, 2015.
- An, M., Wiens, D. A., Zhao, Y., Feng, M., Nyblade, A., Kanao, M., Li, Y., Maggi, A., and L  v  que, J. J.: Temperature,  
lithosphere-asthenosphere boundary, and heat flux beneath the Antarctic Plate inferred from seismic velocities, *Journal of  
605 Geophysical Research: Solid Earth*, 120, 8720-8742, <https://doi.org/10.1002/2015JB011917>, 2015.
- Austermann, J., Mitrovica, J. X., Latychev, K., and Milne, G. A.: Barbados-based estimate of ice volume at Last Glacial  
Maximum affected by subducted plate, *Nature Geoscience*, 6, 553-557, <https://doi.org/10.1038/ngeo1859>, 2013.



- Bamber, J. L. and Dawson, G. J.: Complex evolving patterns of mass loss from Antarctica's largest glacier, *Nature Geoscience*, 13, 127-131, <https://doi.org/10.1038/s41561-019-0527-z>, 2020.
- 610 Barletta, V. R., Bevis, M., Smith, B. E., Wilson, T., Brown, A., Bordoni, A., Willis, M., Khan, S. A., Rovira-Navarro, M., Dalziel, I., Smalley, R., Jr., Kendrick, E., Konfal, S., Caccamise, D. J., 2nd, Aster, R. C., Nyblade, A., and Wiens, D. A.: Observed rapid bedrock uplift in Amundsen Sea Embayment promotes ice-sheet stability, *Science*, 360, 1335-1339, <https://doi.org/10.1126/science.aao1447>, 2018.
- 615 Berger, S., Favier, L., Drews, R., Derwael, J.-J., and Pattyn, F.: The control of an uncharted pinning point on the flow of an Antarctic ice shelf, *Journal of Glaciology*, 62, 37-45, <https://doi.org/10.1017/jog.2016.7>, 2016.
- Carrivick, J. L., Davies, B. J., James, W. H., McMillan, M., and Glasser, N. F.: A comparison of modelled ice thickness and volume across the entire Antarctic Peninsula region, *Geografiska Annaler: Series A, Physical Geography*, 101, 45-67, <https://doi.org/10.1080/04353676.2018.1539830>, 2019.
- 620 Conrad, C. P. and Lithgow-Bertelloni, C.: Influence of continental roots and asthenosphere on plate-mantle coupling, *Geophysical Research Letters*, 33, <https://doi.org/10.1029/2005GL025621>, 2006.
- Cornford, S., Martin, D., Lee, V., Payne, A., and Ng, E.: Adaptive mesh refinement versus subgrid friction interpolation in simulations of Antarctic ice dynamics, *Annals of Glaciology*, 57, 1-9, <https://doi.org/10.1017/aog.2016.13>, 2016.
- De Boer, B., Stocchi, P., and Van De Wal, R.: A fully coupled 3-D ice-sheet–sea-level model: algorithm and applications, *Geoscientific Model Development*, 7, 2141-2156, <https://doi.org/10.5194/gmd-7-2141-2014>, 2014.
- 625 DeConto, R. M., Pollard, D., Alley, R. B., Velicogna, I., Gasson, E., Gomez, N., Sadai, S., Condron, A., Gilford, D. M., Ashe, E. L., Kopp, R. E., Li, D., and Dutton, A.: The Paris Climate Agreement and future sea-level rise from Antarctica, *Nature*, 593, 83-89, <https://doi.org/10.1038/s41586-021-03427-0>, 2021.
- Durand, G., Gagliardini, O., Zwinger, T., Le Meur, E., and Hindmarsh, R. C.: Full Stokes modeling of marine ice sheets: influence of the grid size, *Annals of Glaciology*, 50, 109-114, <https://doi.org/10.3189/172756409789624283>, 2009.
- 630 Durkin IV, W., Wilson, T.J., Hansen, J.S., Willis, M. and Bevis, M.G., 2020, December. Reevaluating the Elastic Response to Ice Mass Change in Antarctica. In AGU Fall Meeting Abstracts (Vol. 2020, pp. G012-0023).
- Favier, L., Gagliardini, O., Durand, G., and Zwinger, T.: A three-dimensional full Stokes model of the grounding line dynamics: effect of a pinning point beneath the ice shelf, *The Cryosphere*, 6, 101-112, <https://doi.org/10.5194/tc-6-101-2012>, 2012.
- 635 Fretwell, P., Pritchard, H.D., Vaughan, D.G., Bamber, J.L., Barrand, N.E., Bell, R., Bianchi, C., Bingham, R.G., Blankenship, D.D., Casassa, G. and Catania, G.: Bedmap2: improved ice bed, surface and thickness datasets for Antarctica. *The Cryosphere*, 7, 375-393, <https://doi.org/10.5194/tc-7-375-2013>, 2013.
- Forte, A.M. and Mitrovica, J.X.: New inferences of mantle viscosity from joint inversion of long-wavelength mantle convection and post-glacial rebound data, *Geophysical Research Letters*, 23, 1147-1150, <https://doi.org/10.1029/96GL00964>, 1996
- 640 Gladstone, R. M., Payne, A. J., and Cornford, S. L.: Resolution requirements for grounding-line modelling: sensitivity to basal drag and ice-shelf buttressing, *Annals of glaciology*, 53, 97-105, <https://doi.org/10.3189/2012AoG60A148>, 2012.
- Golledge, N. R., Keller, E. D., Gomez, N., Naughten, K. A., Bernales, J., Trusel, L. D., and Edwards, T. L.: Global environmental consequences of twenty-first-century ice-sheet melt, *Nature*, 566, 65-72, <https://doi.org/10.1038/s41586-019-0889-9>, 2019.
- 645



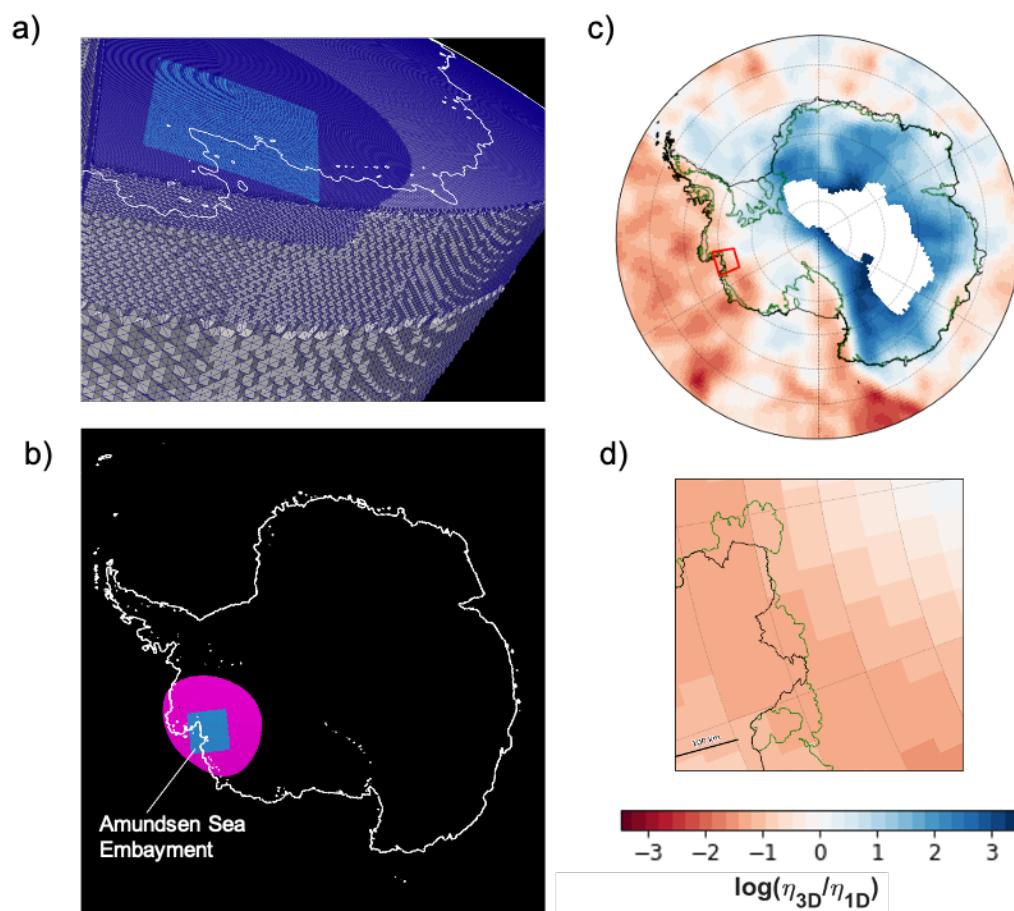
- Gomez, N., Latychev, K., and Pollard, D.: A coupled ice sheet–sea level model incorporating 3D earth structure: variations in Antarctica during the last deglacial retreat, *Journal of Climate*, 31, 4041-4054, <https://doi.org/10.1175/JCLI-D-17-0352.1>, 2018.
- 650 Gomez, N., Mitrovica, J. X., Huybers, P., and Clark, P. U.: Sea level as a stabilizing factor for marine-ice-sheet grounding lines, *Nature Geoscience*, 3, 850-853, <https://doi.org/10.1038/ngeo1012>, 2010.
- Gomez, N., Pollard, D., and Holland, D.: Sea-level feedback lowers projections of future Antarctic Ice-Sheet mass loss, *Nat Commun*, 6, 8798, <https://doi.org/10.1038/ncomms9798>, 2015.
- Gomez, N., Pollard, D., and Mitrovica, J. X.: A 3-D coupled ice sheet–sea level model applied to Antarctica through the last 40 ky, *Earth and Planetary Science Letters*, 384, 88-99, <https://doi.org/10.1016/j.epsl.2013.09.042>, 2013.
- 655 Hay, C. C., Lau, H. C., Gomez, N., Austermann, J., Powell, E., Mitrovica, J. X., Latychev, K., and Wiens, D. A.: Sea level fingerprints in a region of complex Earth structure: The case of WAIS, *Journal of Climate*, 30, 1881-1892, <https://doi.org/10.1175/JCLI-D-16-0388.1>, 2017.
- 660 Heeszel, D. S., Wiens, D. A., Anandakrishnan, S., Aster, R. C., Dalziel, I. W., Huerta, A. D., Nyblade, A. A., Wilson, T. J., and Winberry, J. P.: Upper mantle structure of central and West Antarctica from array analysis of Rayleigh wave phase velocities, *Journal of Geophysical Research: Solid Earth*, 121, 1758-1775, <https://doi.org/10.1002/2015JB012616>, 2016.
- Joughin, I., Smith, B. E., and Medley, B.: Marine ice sheet collapse potentially under way for the Thwaites Glacier Basin, West Antarctica, *Science*, 344, 735-738, <https://doi.org/10.1126/science.1249055>, 2014.
- Kachuck, S. B., Martin, D. F., Bassis, J. N., and Price, S. F.: Rapid viscoelastic deformation slows marine ice sheet instability at Pine Island Glacier, *Geophysical Research Letters*, 47, e2019GL086446, <https://doi.org/10.1029/2019GL086446>, 2020.
- 665 Kaufmann, G., Wu, P., and Ivins, E. R.: Lateral viscosity variations beneath Antarctica and their implications on regional rebound motions and seismotectonics, *Journal of Geodynamics*, 39, 165-181, <https://doi.org/10.1016/j.jog.2004.08.009>, 2005.
- Kendall, R. A., Mitrovica, J. X., and Milne, G. A.: On post-glacial sea level–II. Numerical formulation and comparative results on spherically symmetric models, *Geophysical Journal International*, 161, 679-706, <https://doi.org/10.1111/j.1365-246X.2005.02553.x>, 2005.
- 670 King, M. A., Bingham, R. J., Moore, P., Whitehouse, P. L., Bentley, M. J., and Milne, G. A.: Lower satellite-gravimetry estimates of Antarctic sea-level contribution, *Nature*, 491, 586-589, <https://doi.org/10.1038/nature11621>, 2012.
- Konrad, H., Sasgen, I., Pollard, D., and Klemann, V.: Potential of the solid-Earth response for limiting long-term West Antarctic Ice Sheet retreat in a warming climate, *Earth and Planetary Science Letters*, 432, 254-264, <https://doi.org/10.1016/j.epsl.2015.10.008>, 2015.
- 675 Kustowski, B., Ekström, G., and Dziewoński, A.: Anisotropic shear-wave velocity structure of the Earth's mantle: A global model, *Journal of Geophysical Research: Solid Earth*, 113, <https://doi.org/10.1029/2007JB005169>, 2008.
- Ivins, E.R. and Sammis, C.G.: On lateral viscosity contrast in the mantle and the rheology of low-frequency geodynamics. *Geophysical Journal International*, 123, 305-322, <https://doi.org/10.1111/j.1365-246X.1995.tb06856.x>, 1995.
- 680 Lambeck, K., Rouby, H., Purcell, A., Sun, Y., and Sambridge, M.: Sea level and global ice volumes from the Last Glacial Maximum to the Holocene, *Proc Natl Acad Sci U S A*, 111, 15296-15303, <https://doi.org/10.1073/pnas.1411762111>, 2014.
- Larour, E., Seroussi, H., Adhikari, S., Ivins, E., Caron, L., Morlighem, M., and Schlegel, N.: Slowdown in Antarctic mass loss from solid Earth and sea-level feedbacks, *Science*, 364, <https://doi.org/10.1126/science.aav7908>, 2019.



- 685 Latychev, K., Mitrovica, J. X., Tromp, J., Tamisiea, M. E., Komatitsch, D., and Christara, C. C.: Glacial isostatic adjustment on 3-D Earth models: a finite-volume formulation, *Geophysical Journal International*, 161, 421-444, <https://doi.org/10.1111/j.1365-246X.2005.02536.x>, 2005.
- Lloyd, A., Wiens, D., Zhu, H., Tromp, J., Nyblade, A., Aster, R., Hansen, S., Dalziel, I., Wilson, T., and Ivins, E.: Seismic structure of the Antarctic upper mantle imaged with adjoint tomography, *Journal of Geophysical Research: Solid Earth*, 125, <https://doi.org/10.1029/2019JB017823>, 2020.
- 690 Martín-Español, A., Zammit-Mangion, A., Clarke, P.J., Flament, T., Helm, V., King, M.A., Luthcke, S.B., Petrie, E., Rémy, F., Schön, N. and Wouters, B.: Spatial and temporal Antarctic Ice Sheet mass trends, glacio-isostatic adjustment, and surface processes from a joint inversion of satellite altimeter, gravity, and GPS data, *Journal of Geophysical Research: Earth Surface*, 121, 182-200, <https://doi.org/10.1002/2015JF003550>, 2016.
- Mitrovica, J. and Forte, A.: A new inference of mantle viscosity based upon joint inversion of convection and glacial isostatic adjustment data, *Earth and Planetary Science Letters*, 225, 177-189, <https://doi.org/10.1016/j.epsl.2004.06.005>, 2004.
- 695 Morelli, A. and Danesi, S.: Seismological imaging of the Antarctic continental lithosphere: a review, *Global and Planetary Change*, 42, 155-165, <https://doi.org/10.1016/j.gloplacha.2003.12.005>, 2004.
- Morlighem, M., Rignot, E., Binder, T., Blankenship, D., Drews, R., Eagles, G., Eisen, O., Ferraccioli, F., Forsberg, R., and Fretwell, P.: Deep glacial troughs and stabilizing ridges unveiled beneath the margins of the Antarctic ice sheet, *Nature Geoscience*, 13, 132-137, <https://doi.org/10.1038/s41561-019-0510-8>, 2020.
- 700 NOAA National Geophysical Data Centre: 2-minute gridded global relief data (ETOPO2) v2, 2006.
- Nield, G. A., Barletta, V. R., Bordoni, A., King, M. A., Whitehouse, P. L., Clarke, P. J., Domack, E., Scambos, T. A., and Berthier, E.: Rapid bedrock uplift in the Antarctic Peninsula explained by viscoelastic response to recent ice unloading, *Earth and Planetary Science Letters*, 397, 32-41, <https://doi.org/10.1016/j.epsl.2014.04.019>, 2014.
- 705 Nowicki, S. M. J., Payne, T., Larour, E., Seroussi, H., Goelzer, H., Lipscomb, W., Gregory, J., Abe-Ouchi, A., and Shepherd, A.: Ice Sheet Model Intercomparison Project (ISMIP6) contribution to CMIP6, *Geosci Model Dev*, 9, 4521-4545, <https://doi.org/10.5194/gmd-9-4521-2016>, 2016.
- Paterson, W. and Colbeck, S.: Ice sheets and ice shelves, in: *Dynamics of snow and ice masses*, Academic Press, 1-78, 1980.
- Pattyn, F., Perichon, L., Durand, G., Favier, L., Gagliardini, O., Hindmarsh, R. C., Zwinger, T., Albrecht, T., Cornford, S., and Docquier, D.: Grounding-line migration in plan-view marine ice-sheet models: results of the ice2sea MISIP3d intercomparison, *Journal of Glaciology*, 59, 410-422, <https://doi.org/10.3189/2013JoG12J129>, 2013.
- Pollitz, F. F.: Lithosphere and shallow asthenosphere rheology from observations of post-earthquake relaxation, *Physics of the Earth and Planetary Interiors*, 293, 106271, <https://doi.org/10.1016/j.pepi.2019.106271>, 2019.
- 715 Powell, E., Gomez, N., Hay, C., Latychev, K., and Mitrovica, J.: Viscous effects in the solid Earth response to modern Antarctic ice mass flux: Implications for geodetic studies of WAIS stability in a warming world, *Journal of Climate*, 33, 443-459, <https://doi.org/10.1175/JCLI-D-19-0479.1>, 2020.
- Rignot, E., Mouginot, J., Scheuchl, B., van den Broeke, M., van Wessem, M. J., and Morlighem, M.: Four decades of Antarctic Ice Sheet mass balance from 1979-2017, *Proc Natl Acad Sci U S A*, 116, 1095-1103, <https://doi.org/10.1073/pnas.1812883116>, 2019.



- 720 Ritsema, J., Deuss, a. A., Van Heijst, H., and Woodhouse, J.: S40RTS: a degree-40 shear-velocity model for the mantle from new Rayleigh wave dispersion, teleseismic traveltime and normal-mode splitting function measurements, *Geophysical Journal International*, 184, 1223-1236, <https://doi.org/10.1111/j.1365-246X.2010.04884.x>, 2011.
- Ritzwoller, M. H., Shapiro, N. M., Levshin, A. L., and Leahy, G. M.: Crustal and upper mantle structure beneath Antarctica and surrounding oceans, *Journal of Geophysical Research: Solid Earth*, 106, 30645-30670, <https://doi.org/10.1029/2001JB000179>, 2001.
- 725 Schröder, L., Horwath, M., Dietrich, R., Helm, V., Broeke, M. R., and Ligtenberg, S. R.: Four decades of Antarctic surface elevation changes from multi-mission satellite altimetry, *The Cryosphere*, 13, 427-449, <https://doi.org/10.5194/tc-13-427-2019>, 2019.
- Seroussi, H., Nowicki, S., Payne, A. J., Goelzer, H., Lipscomb, W. H., Abe-Ouchi, A., Agosta, C., Albrecht, T., Asay-Davis, X., and Barthel, A.: ISMIP6 Antarctica: a multi-model ensemble of the Antarctic ice sheet evolution over the 21st century, *The Cryosphere*, 14, 3033-3070, <https://doi.org/10.5194/tc-14-3033-2020>, 2020.
- 730 Shen, W., Wiens, D. A., Anandakrishnan, S., Aster, R. C., Gerstoft, P., Bromirski, P. D., Hansen, S. E., Dalziel, I. W., Heeszel, D. S., and Huerta, A. D.: The crust and upper mantle structure of central and West Antarctica from Bayesian inversion of Rayleigh wave and receiver functions, *Journal of Geophysical Research: Solid Earth*, 123, 7824-7849, <https://doi.org/10.1029/2017JB015346>, 2018.
- 735 Shepherd, A., Gilbert, L., Muir, A. S., Konrad, H., McMillan, M., Slater, T., Briggs, K. H., Sundal, A. V., Hogg, A. E., and Engdahl, M. E.: Trends in Antarctic Ice Sheet elevation and mass, *Geophysical Research Letters*, 46, 8174-8183, <https://doi.org/10.1029/2019GL082182>, 2019.
- Smith, B., Fricker, H. A., Gardner, A. S., Medley, B., Nilsson, J., Paolo, F. S., Holschuh, N., Adusumilli, S., Brunt, K., Csatho, B., Harbeck, K., Markus, T., Neumann, T., Siegfried, M. R., and Zwally, H. J.: Pervasive ice sheet mass loss reflects competing ocean and atmosphere processes, *Science*, 368, 1239-1242, <https://doi.org/10.1126/science.aaz5845>, 2020.
- 740 Spada, G. and Stocchi, P.: SELEN: A Fortran 90 program for solving the “sea-level equation”, *Computers & Geosciences*, 33, 538-562, <https://doi.org/10.1016/j.cageo.2006.08.006>, 2007.
- Studinger, M.: IceBridge ATM L4 surface elevation rate of change, NASA National Snow and Ice Data Center Distributed Active Archive Center, Boulder, Colorado USA, 10, 2014.
- 745 The IMBIE team: Mass balance of the Antarctic Ice Sheet from 1992 to 2017. *Nature* 558, 219–222, <https://doi.org/10.1038/s41586-018-0179-y>, 2018.
- Van den Berg, J., Van de Wal, R., and Oerlemans, J.: Effects of spatial discretization in ice-sheet modelling using the shallow-ice approximation, *Journal of glaciology*, 52, 89-98, <https://doi.org/10.3189/172756506781828935>, 2006.
- 750 van der Wal, W., Whitehouse, P. L., & Schrama, E. J.: Effect of GIA models with 3D composite mantle viscosity on GRACE mass balance estimates for Antarctica, *Earth and Planetary Science Letters*, 414, 134-143, <https://doi.org/10.1016/j.epsl.2015.01.001>, 2015.
- Zhao, C., King, M. A., Watson, C. S., Barletta, V. R., Bordoni, A., Dell, M., and Whitehouse, P. L.: Rapid ice unloading in the Fleming Glacier region, southern Antarctic Peninsula, and its effect on bedrock uplift rates, *Earth and Planetary Science Letters*, 473, 164-176, <https://doi.org/10.1016/j.epsl.2017.06.002>, 2017.
- 755 Zwinger, T., Nield, G. A., Ruokolainen, J., and King, M. A.: A new open-source viscoelastic solid earth deformation module implemented in Elmer (v8. 4), *Geoscientific Model Development*, 13, 1155-1164, <https://doi.org/10.5194/gmd-13-1155-2020>, 2020.



760

765

770

**Figure 1. Grid and Earth model configuration. (a-b) Configuration of the tetrahedral grid in the finite-volume 3-D GIA model with regional refinement, used for observational and modelled ice loading scenarios. (a) shows a cross-sectional view of the regional refinement along ASE. (b) indicates areas of grid refinement across Antarctica with a surface grid resolution of 7.5 km over all Antarctica in black, 3.75 km over a section of the West Antarctica in magenta and 1.9 km in the ASE (light blue square). (c-d) Logarithmic viscosity perturbation map at depth 200 km for low upper mantle viscosity model EM1\_L over (c) Antarctica and (d) our study region in the Amundsen Sea Embayment. Values are relative to reference 1-D model with upper mantle viscosity of  $1 \times 10^{20}$  Pa s, and lower mantle viscosity of  $5 \times 10^{21}$  Pa s. The black line delimits the Antarctic grounding line, and the dark green line shows the bedrock topography contour at 0 m from Bedmap2 (Fretwell et al., 2013) highlighting marine-based sectors of ice.**

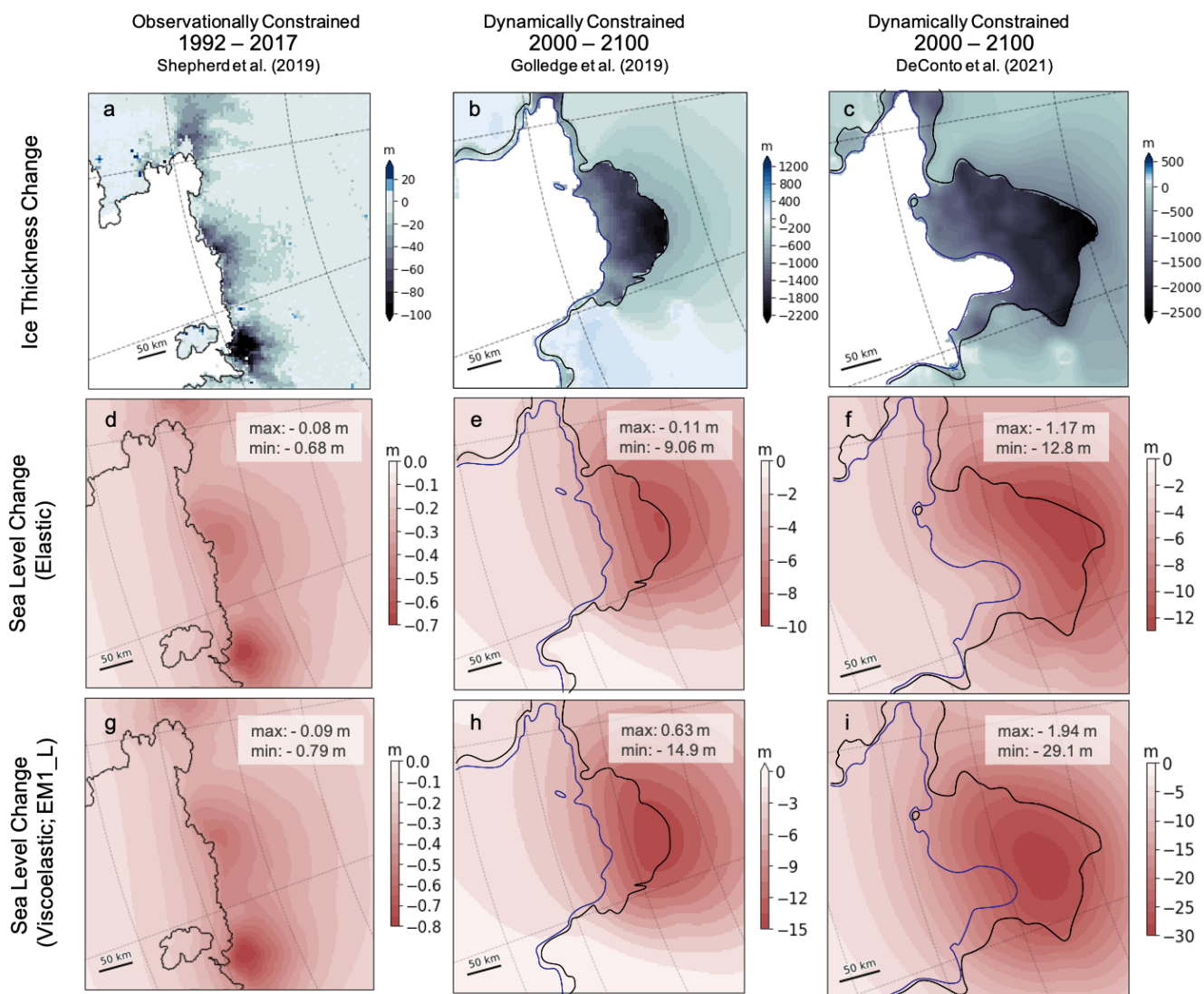
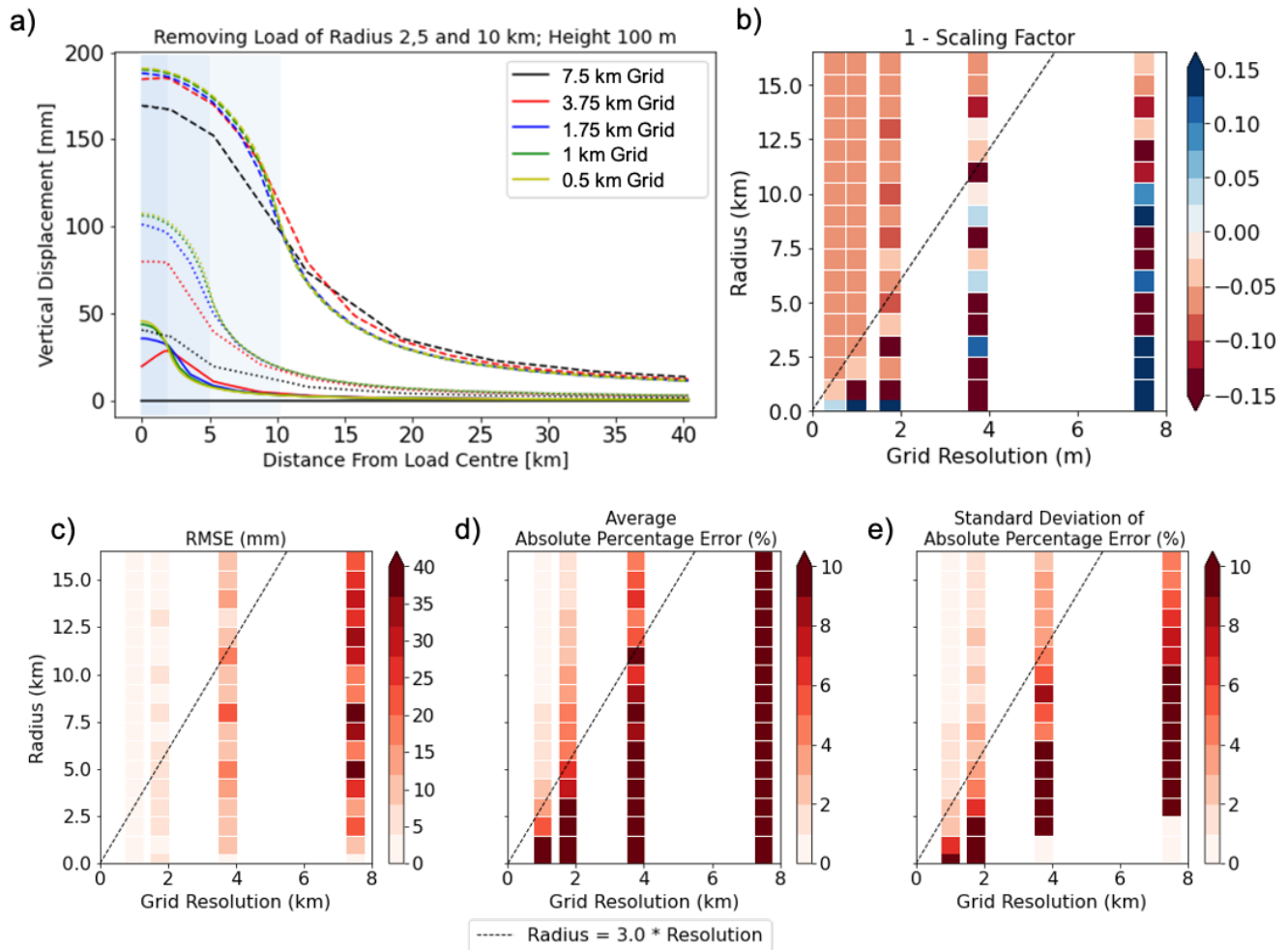


**Figure 2.** Ice loading scenarios and corresponding elastic sea level predictions in the ASE. (a – c) Total ice thickness change in meters predicted from (a) 1997 to 2017 in the observation-based ICE-SH ice model (Shepherd et al., 2019), and from 2000 to 2100 in the (b) ICE-GOL (Golledge et al., 2019) and ICE-RD (DeConto et al., 2021) ice model projections. (d – f) show the predicted sea level change in meters with an elastic earth model associated with the ice cover changes shown in (a–c). (g– i) as in (d–f) but adopting 3-D viscoelastic earth model EM1\_L. The black and blue line indicates final and initial grounding lines, respectively, for each simulation. Each frame is annotated with the maximum and minimum value within the frame. Note that the colour bars change across each frame.

775

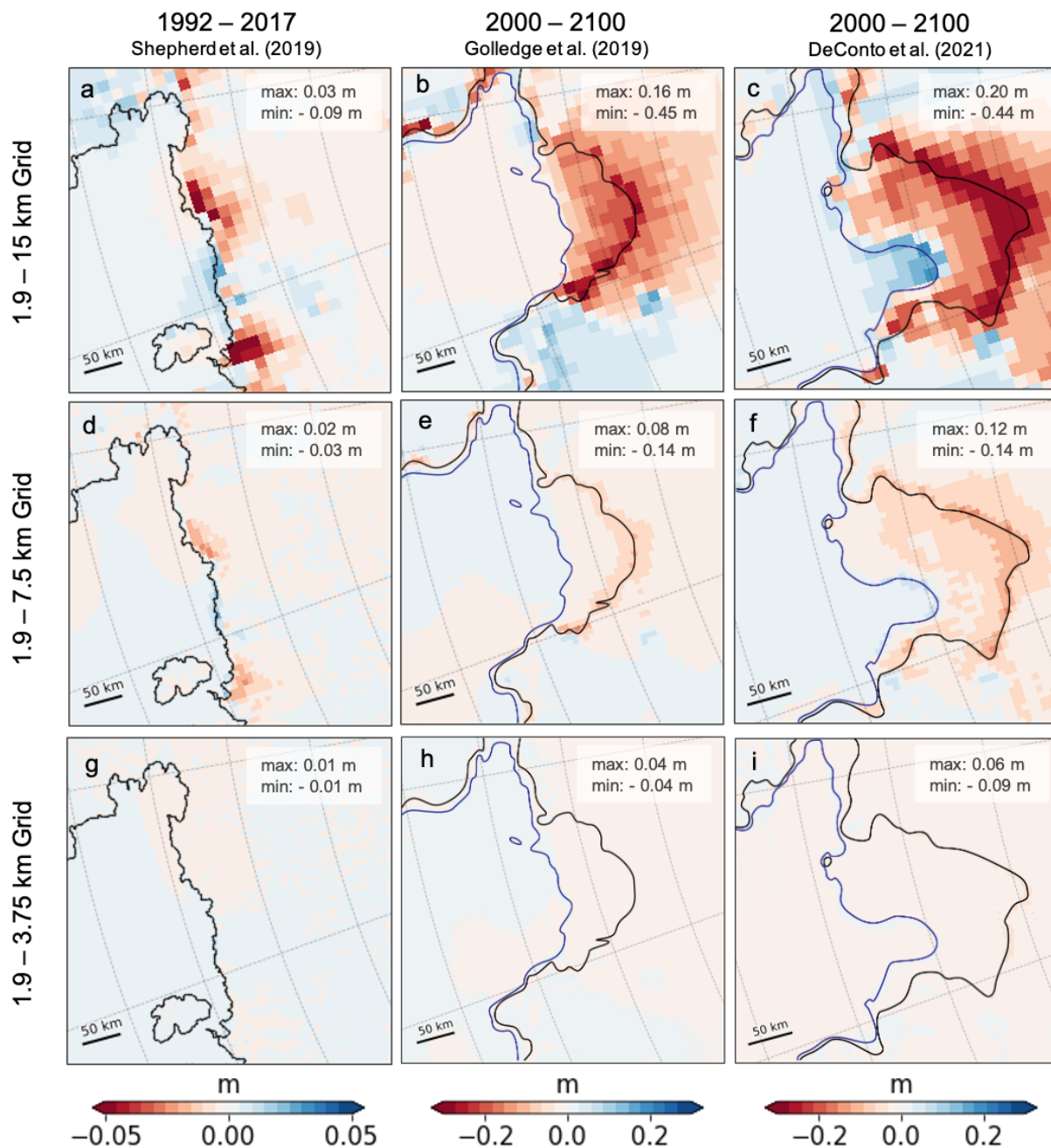


780

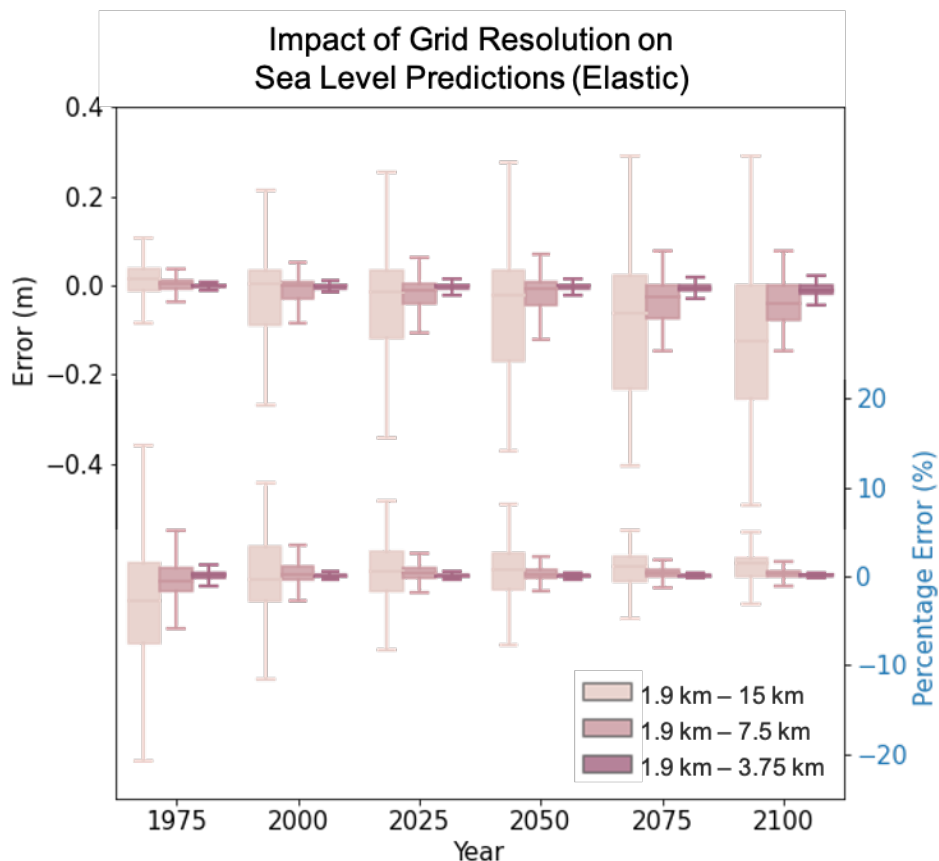
Figure 3. Idealized sensitivity experiment of the effect of surface grid resolution on GIA model calculations with elastic bedrock deformation due to instantaneous removal of cylindrical ice loads. Cylinders are all of unit height 100 m, and radius from 0.5 to 16 km. Five grid resolutions applied within an area of minimum 40km width were tested: 0.5, 1, 1.75 km, 3.75 and 7.5 km (Figure S1). (a) Transect of bedrock deformation for removal of ice cylinders with unit height and radii of 2 km (solid lines), 5 km (dotted) and 10 km (dashed lines). (b) – (e) Results of a suite of simulations adopting ranges of ice cylinder radii and grid resolutions. (b) Colors indicate 1 minus the Scaling Factor,  $[1 - \text{Scaling Factor}]$ , where the Scaling Factor is the ratio of the theoretical mass of the load and the mass of the load represented on the given model grid. 0 represents a scenario where the model grid perfectly represents the mass of the idealized load, whilst positive (blue) and negative (red) values indicate the load mass is over- and under-represented by model grid resolution, respectively. (c) Root mean square error across the suite of simulations (mm). (d) Average absolute percentage error (%). (e) Standard deviation of the absolute percentage error (%) of the given test from the finest 0.5 km resolution model result, calculated within 2 km of the loaded region. Dashed black lines represent the 1:3 ratio between idealized load cylinder radius and surface grid resolution whereby average absolute percentage error becomes  $< 7 \pm 3 (\sigma) \%$  for all scenarios.

785

790



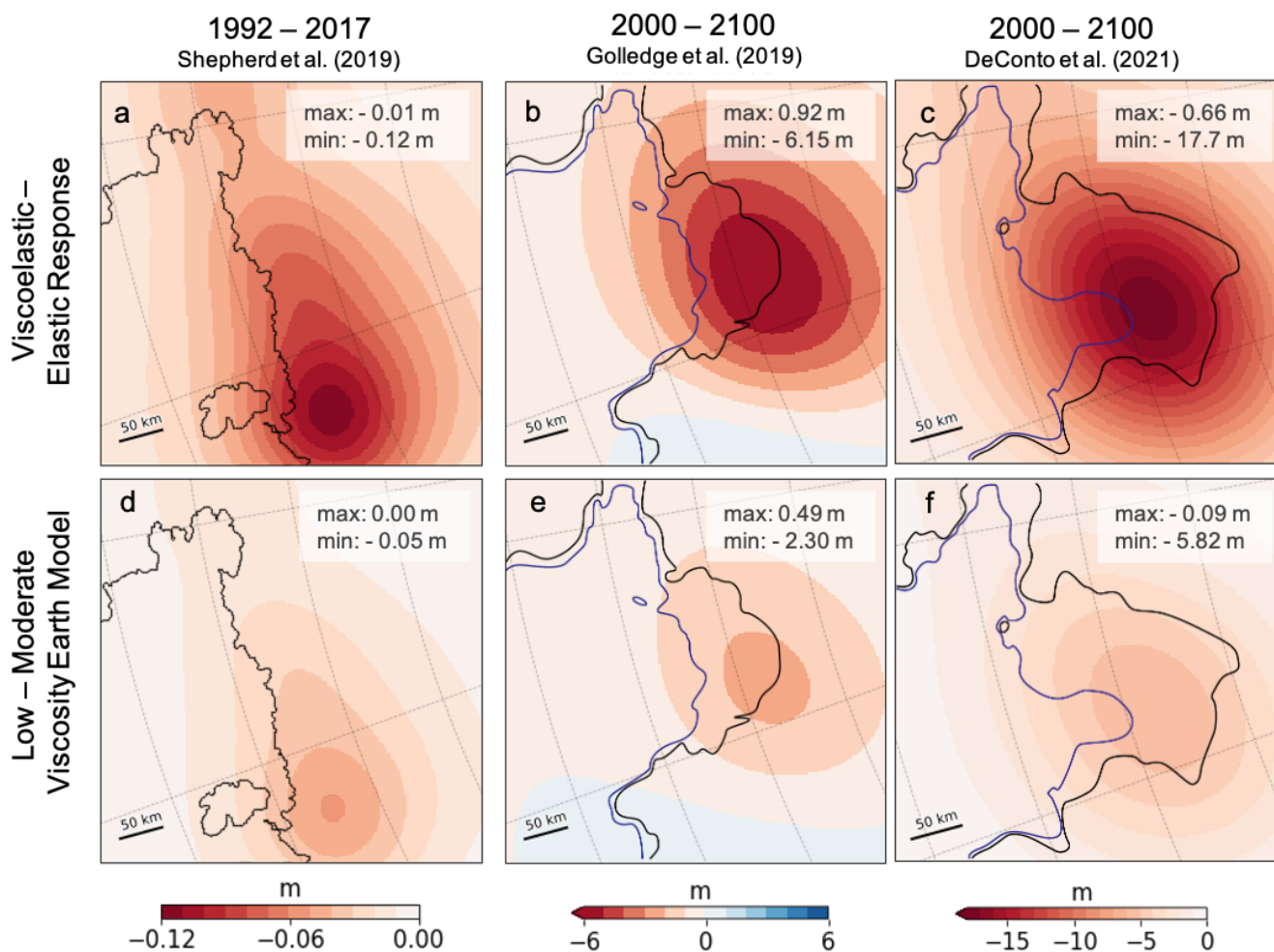
795 **Figure 4.** Influence of grid resolution on elastic sea level predictions in ASE. Difference in predicted sea level change in meters between (a-c) 1.9 and 15 km, (d-f) 1.9 and 7.5 km; and (g-i) 1.9 and 3.75 km resolution GIA model simulations with a purely elastic Earth model across the times indicated at the top of the column for ice loading scenarios (from left – right) ICE-SH ICE-GOL and ICE-RD. For each ice retreat scenario there is a different colour bar since the magnitude of error due to grid resolution differs. In some panels, the colour bar is saturated. The black and blue line indicates final and initial grounding lines, respectively, for each simulation, and each frame is annotated with the maximum and minimum values within the frame.



800

805

**Figure 5. Evolution of error in elastic sea level predictions due to grid resolution from 1950 to 2100 with the 1km input resolution ICE-RD ice model. (a) Box-whisker plots of the error and percent error (see methods) calculated from the difference in predicted sea level changes from the start of the simulation to the indicated time within 10 km of the grounding line at that time between a simulation with 1.9 km resolution and simulations adopting 15 km (light pink), 7.5 km (medium pink) and 3.75 km (dark pink) grid resolutions. The box represents (from left to right) the 25th percentile, median and 75th percentile of the distribution, whilst the whiskers represent the "minimum" (25th percentile - 1.5 x the interquartile range) and "maximum" (75th percentile + 1.5 x the interquartile range). Error (m) is the difference between sea-level predictions from the higher - lower resolution run. Percentage Error (%) is calculated as  $100 * (SL_{1.9km} - SL_{lowres}) / SL_{1.9km}$  for each grid point.**



810 **Figure 6. Influence of incorporating viscous behaviour and uncertainty in viscoelastic Earth structure on sea level predictions.**  
 Frames (a-c) shows the difference in sea level change predicted from simulations adopting 3-D viscoelastic earth model EM1\_L and  
 an elastic Earth model. Frames (d-f) shows the difference in sea level change predicted from simulations adopting two different 3-D  
 viscoelastic earth models EM1\_L and EM1\_M. Note the difference in scale. Time frames and ice models are as indicated at the top  
 of the columns. In each frame, the black and blue line indicates final and initial grounding lines respectively for each simulation  
 815 and is annotated with the maximum and minimum data value within the frame. All simulations adopt a 1.9 km grid resolution.

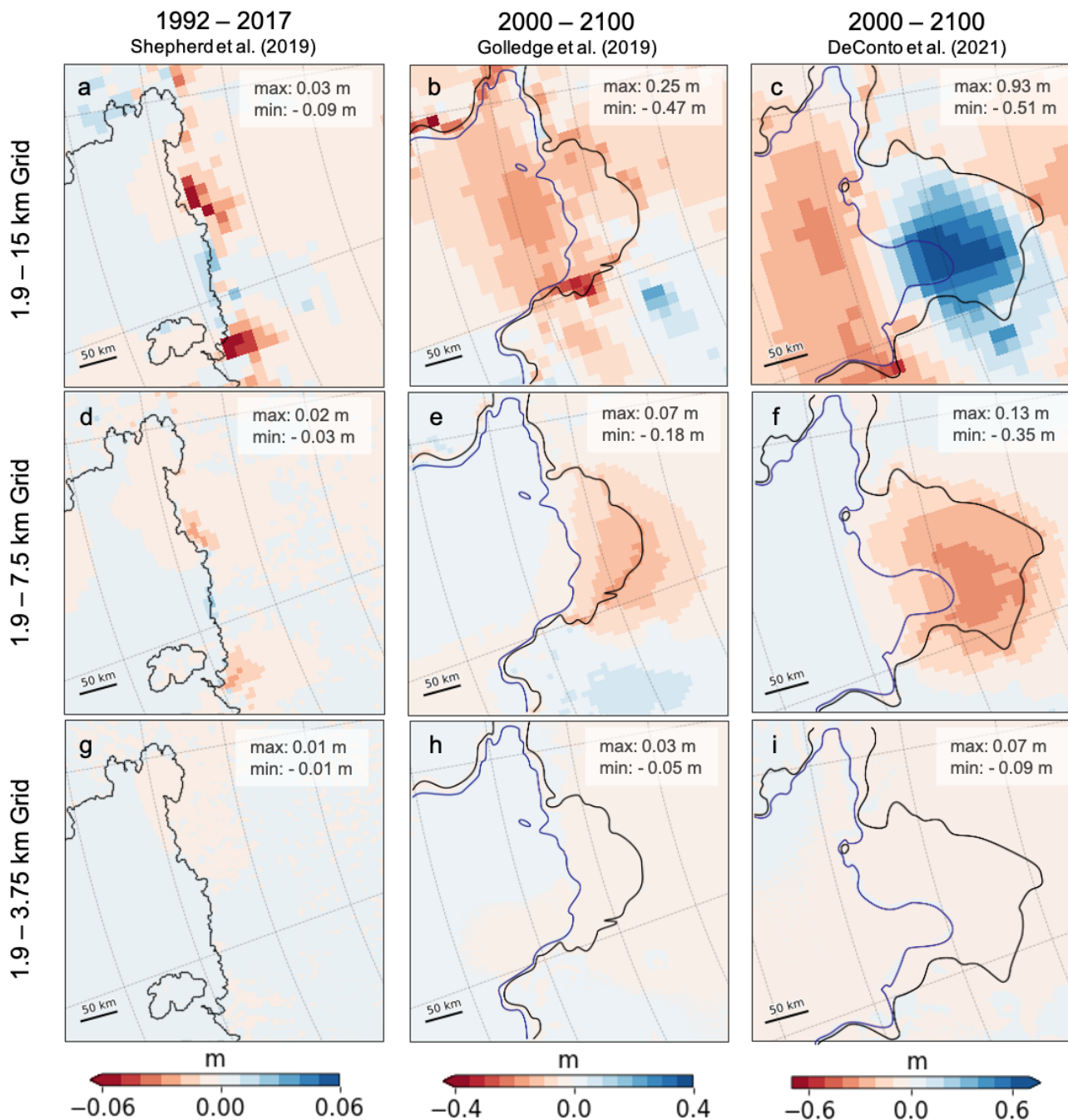
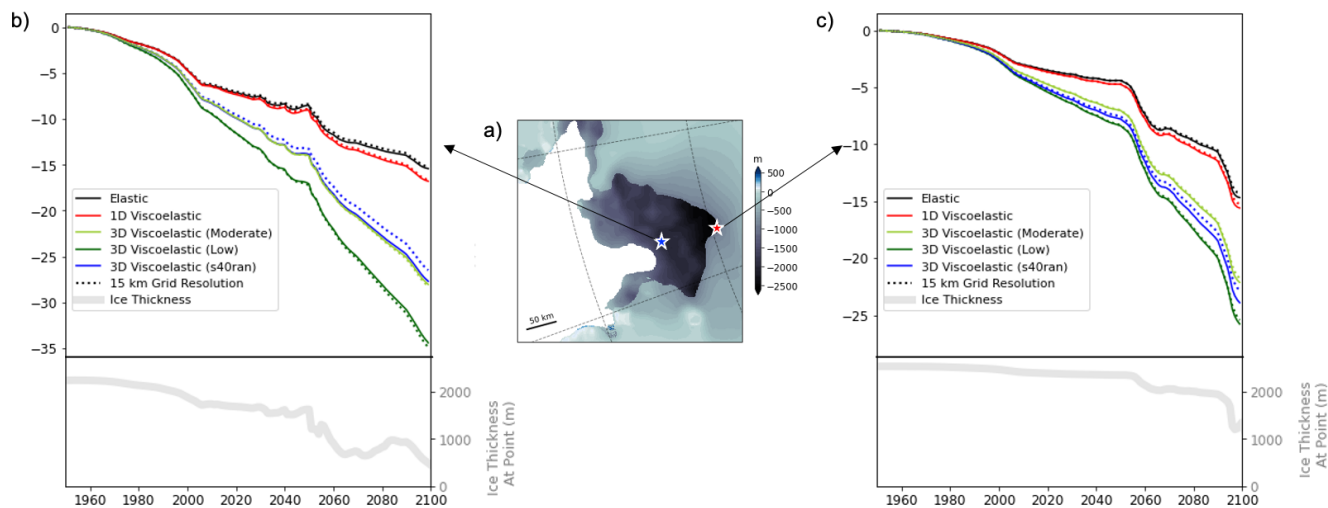


Figure 7. Influence of grid resolution on viscoelastic sea level predictions in ASE. As in Figure 4 but adopting 3-D viscoelastic Earth model EM1\_L.



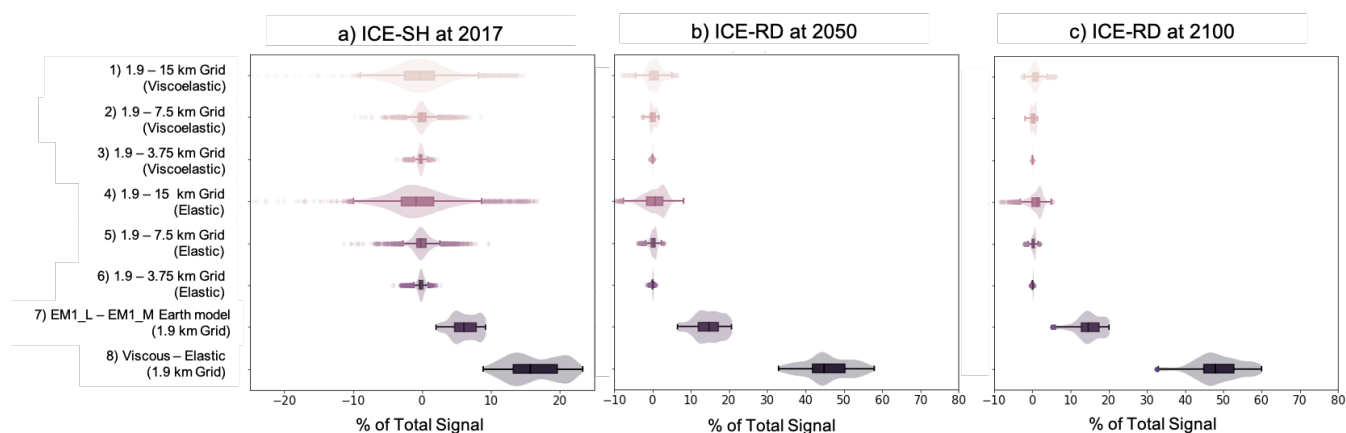
820

825

**Figure 8. Evolution of site-specific sea level in simulations adopting a range of model resolutions and Earth models. (a) ice thickness change from 2000 to 2100 predicted in the ICE-RD simulation. This frame is identical to figure 3c. (b) colored lines show predicted sea level change, in meters, at the site that experiences the maximum viscous uplift in the 1.9 km resolution simulation, shown by the blue star in frame (a) in the simulations with a purely elastic solid earth response (black lines), viscoelastic solid earth response based on a 1-D earth model (red lines), a low viscosity 3-D earth model EM1\_L (dark green lines), a moderate viscosity 3-D earth model EM1\_M (light green lines) and 3-D viscosity earth model EM2 (blue lines). Solid lines are for simulations performed at 1.9 km resolution, and dashed lines adopt a 15km resolution. (c) is as in frame (b) but for the site along the final grounding line position at 2100 that experiences the greatest ice thickness change, labeled by the red star in frame (a).**



830



835

**Figure 9. Comparison of factors contributing to differences in sea-level predictions in this study. Each distribution represents the influence of the specific factor across points within 10-km of the grounding line at the specified year of the model run, as a percentage of the total sea-level change at that time for a) ICE-SH ice model from 1992 to 2017; b) ICE-RD ice model from 1950 to 2050; c) ICE-RD ice model from 1950 to 2100. Six factors are compared in this figure, as labelled on the right. To visualise the distribution, we plot a classic box-whisker diagram overlain with a density curve. The box represents (from left to right) the 25<sup>th</sup> percentile, median and 75<sup>th</sup> percentile of the distribution, whilst the whiskers represent the “minimum” (25<sup>th</sup> percentile – 1.5 x the interquartile range) and “maximum” (75<sup>th</sup> percentile + 1.5 x the interquartile range). The diamonds outside the whiskers represent outliers.**

840